Sorting nexin 27 couples PTHR trafficking to retromer for signal regulation in osteoblasts during bone growth

Audrey S. M. Chan[a], Thomas Clairfeuille[b], Euphemie Landao-Bassonga[a], Genevieve Kinna[b], Pei Ying Ng[a], Li Shen Loo[c], Tak Sum Cheng[a], Minghao Zheng[a], Wanjin Hong[c], Rohan D. Teasdale[b], Brett M. Collins[b,†,*], and Nathan J. Pavlos[a,†,*]

[a]Cellular Orthopaedic Laboratory, School of Surgery, University of Western Australia, Nedlands 6009, Australia; [b]Institute for Molecular Bioscience, University of Queensland, St. Lucia 4072, Australia; [c]Institute of Molecular and Cell Biology, A*STAR, Singapore 138673

ABSTRACT **The parathyroid hormone 1 receptor (PTHR) is central to the process of bone formation and remodeling. PTHR signaling requires receptor internalization into endosomes, which is then terminated by recycling or degradation. Here we show that sorting nexin 27 (SNX27) functions as an adaptor that couples PTHR to the retromer trafficking complex. SNX27 binds directly to the C-terminal PDZ-binding motif of PTHR, wiring it to retromer for endosomal sorting. The structure of SNX27 bound to the PTHR motif reveals a high-affinity interface involving conserved electrostatic interactions. Mechanistically, depletion of SNX27 or retromer augments intracellular PTHR signaling in endosomes. Osteoblasts genetically lacking SNX27 show similar disruptions in PTHR signaling and greatly reduced capacity for bone mineralization, contributing to profound skeletal deficits in SNX27-knockout mice. Taken together, our data support a critical role for SNX27-retromer mediated transport of PTHR in normal bone development.**

Monitoring Editor
Adam Linstedt
Carnegie Mellon University

Received: Dec 22, 2015
Revised: Feb 5, 2016
Accepted: Feb 10, 2016

INTRODUCTION

Growth and refurbishment of the vertebrate skeleton are strictly dependent on the coordinated cross-talk between bone-resident cells and their ability to respond to external stimuli via cell surface signaling receptors (Kronenberg, 2003; Sims and Martin, 2014). The type 1 parathyroid hormone receptor (PTHR), a member of the class B G protein–coupled receptor (GPCR) family, is one of the best characterized and most important signaling receptors, modulating bone remodeling and mineral ion homeostasis (Gardella and Vilardaga, 2015). In mammals, PTHR is primarily present in bone cells and kidney proximal tubules, where it elicits its physiological function(s) in blood calcium and phosphate metabolism and tissue development through the endocrine and paracrine/autocrine actions of two distinct peptide ligands, PTH and PTH-related protein (PTHrP; McCauley and Martin, 2012; Gardella and Vilardaga, 2015). Not surprisingly, abnormal expression and/or function of PTHR correspond with severe bone dysmorphisms (termed skeletal dysplasia) and various metabolic syndromes in both humans and mice (Karaplis and Goltzman, 2000). Specifically, disruption in PTHR signaling affects differentiation of cartilage-synthesizing chondrocytes and bone-forming osteoblasts (OBs), leading to alterations in postnatal growth and development of skeletal long bones. Intermittent injection of a PTH analogue is used in the clinical management of osteoporosis. Thus factors that influence PTH signaling are highly sought after for the development of new therapeutic targets for the treatment of osteoporosis and other metabolic bone and mineral diseases (Martin and Seeman, 2007; Kraenzlin and Meier, 2011).

PTH is released by the parathyroid gland in response to low serum calcium levels, which stimulate PTHR in OBs and activate parallel signaling pathways through trimeric G protein subunits $G\alpha_s$ and

This article was published online ahead of print in MBoC in Press (http://www.molbiolcell.org/cgi/doi/10.1091/mbc.E15-12-0851) on February 24, 2016.

†These should be considered co–senior authors.

*Address correspondence to: Nathan Pavlos (nathan.pavlos@uwa.edu.au), Brett Collins (b.collins@imb.uq.edu.au).

Abbreviations used: EEA1, early endosome antigen-1; FYVE, Fab1p/YOTB/Vac1/EEA1; GPCR, G protein–coupled receptor; LAMP-1, lysosomal integral membrane protein; OB, osteoblast; PDZ, postsynaptic density 95/discs large/zonula occludens-1; PDZbm, PDZ-binding motif; PTH, parathyroid hormone; PTHR, PTH type 1 receptor; PTHrP, PTH-related protein; SNX, sorting nexin; VPS, vacuolar protein sorting.

$G\alpha_q$. The $G\alpha_q$ cascade activates phospholipase C, leading to inositol-(1,4,5)-trisphosphate production, elevated Ca^{2+}, protein kinase C (PKC) activation, and subsequent mitogen-activated protein kinase (MAPK)–mediated cell proliferation. $G\alpha_s$ activates adenylyl cyclases to produce cAMP, stimulating the protein kinase A (PKA) pathway, transcription factor activation, and production of receptor activator of NF-κB ligand (RANKL), eventually stimulating RANK-expressing osteoclasts (bone-degrading cells). These signaling cascades in OBs result in the phosphorylation of downstream targets, most notably cAMP-response element-binding protein (CREB), the kinase AKT, and MAPKs, including extracellular signal–regulated kinases ERK1/2. As with other GPCRs, PTHR-evoked cAMP production has long been believed to originate almost exclusively at the cell membrane, with signal termination achieved upon receptor phosphorylation via G protein receptor kinases, β-arrestin–mediated internalization into early endosomes, and lysosomal degradation, that is, "canonical" GPCR signaling (Lohse *et al.*, 1992; Ferrari *et al.*, 1999; Bisello *et al.*, 2002; Chauvin *et al.*, 2002; Bouxsein *et al.*, 2005). However, it is now known that cAMP accumulation persists long after PTHR is internalized into endosomes (Ferrandon *et al.*, 2009). This "noncanonical" endosomal GPCR signaling involves an elaborate ensemble of proteins, which function to promote PTHR-mediated cAMP accumulation, including G proteins, β-arrestins, and small Rab GTPases (Rab5), which facilitate endocytosis and trafficking of the receptor to early endosomes (Vilardaga *et al.*, 2012). Here cAMP generation persists until final signal arrest from the receptor upon PKA-driven intraluminal acidification and the recruitment of the retromer protein complex (Ferrandon *et al.*, 2009; Feinstein *et al.*, 2011; Gidon *et al.*, 2014).

Retromer is an evolutionarily conserved endosomal protein complex composed of a trimeric core consisting of vacuolar protein sorting 26 (VPS26), VPS29, and VPS35 (Collins, 2008). Retromer plays a central role in endosomal membrane trafficking and is best recognized for regulating retrograde endosome-to–*trans*-Golgi network (TGN) trafficking of transmembrane cargoes (Seaman, 2012; Gallon and Cullen, 2015). Recently, however, it has been shown that retromer plays an equally important role in recycling of endocytosed protein to the plasma membrane (PM) via a complex with sorting nexin 27 (SNX27; Temkin *et al.*, 2011; Steinberg *et al.*, 2013). SNX27 is a member of a large family of proteins containing a membrane-binding phox homology domain that controls endosomal recruitment (Cullen and Korswagen, 2012; Teasdale and Collins, 2012). It also possesses a C-terminal 4.1/ezrin/moesin/radixin (FERM)–like domain that mediates binding to transmembrane cargoes containing F-x-N-P-x-Y sequences (Ghai *et al.*, 2011, 2013) and a unique N-terminal postsynaptic density 95/discs large/zonula occludens-1 (PDZ) domain. The PDZ domain binds to type 1 PDZ-binding motifs (PDZbms) with the consensus [TS]-x-ϕ (where ϕ is a bulky hydrophobic amino acid) to mediate endosomal trafficking (Joubert *et al.*, 2004; Lunn *et al.*, 2007; Lauffer *et al.*, 2010; Balana *et al.*, 2011; Cai *et al.*, 2011; Temkin *et al.*, 2011; Valdes *et al.*, 2011; Hayashi *et al.*, 2012; Wang *et al.*, 2013; Loo *et al.*, 2014). SNX27 and retromer form a complex to mediate the trafficking of many PDZbm-containing cargoes, and cargo interactions with SNX27 are allosterically enhanced by the retromer subunit VPS26 binding directly to the PDZ domain (Steinberg *et al.*, 2013; Gallon *et al.*, 2014). Although SNX27–retromer disruption has been associated with neuronal defects in mouse models and human disease (Muhammad *et al.*, 2008; Cai *et al.*, 2011; Vilarino-Guell *et al.*, 2011; Zimprich *et al.*, 2011; Wang *et al.*, 2013, 2014; Loo *et al.*, 2014; Damseh *et al.*, 2015), the range of cargoes bound by the SNX27–retromer complex (Steinberg *et al.*, 2013) points to a much broader physiological role.

Here we use a broad range of structural and cellular approaches combined with mouse knockout models to demonstrate that the SNX27–retromer complex plays a central role in PTHR signaling and retromer-mediated endosomal recycling during bone growth and remodeling in vivo. PTHR is coupled to the retromer complex via the structurally unique SNX27 PDZ domain. We show that the assembly of this complex occurs on endosomes in response to PTH stimulation, where it directs PTHR to retromer for recycling to the cell surface, and provide evidence that the PTHR-SNX27-retromer association is physiologically required to restrict PTH signaling in OBs, where disruption of SNX27 impairs OB activity and contributes to a severe growth and maturation deficit in the skeleton of SNX27-deficient mice. Thus we propose that SNX27 serves as an endosomal PDZ-cargo adaptor that links PTHR to the retromer trafficking complex to regulate PTHR signaling during postnatal bone development.

RESULTS

SNX27 PDZ domain interacts with PTHR in endosomes after PTH stimulation

The type 1 PDZ motif (-T-V-M) encoded at the C-terminus of PTHR is highly conserved across species and similar to other known SNX27-PDZ–binding proteins including the potassium channel Kir3.3, making PTHR a potential SNX27-PDZ–interacting cargo (Figure 1, A and B). To test this, we coexpressed C-terminal green fluorescent protein (GFP)–tagged full-length (FL) and mutant variants of SNX27 lacking either the entire PDZ-domain (ΔPDZ) or a single–amino acid point substitution (H114A) known to destabilize PDZ-associated SNX27 cargoes (Lauffer *et al.*, 2010; Gallon *et al.*, 2014) in a human embryonic kidney cell (HEK293) clone stably expressing myc-tagged PTHR (Figure 1, C and D) and coimmunoprecipitated the resulting complexes using anti-GFP coated beads (GFP-TRAP). We chose HEK293 cells exogenously expressing PTHR as a model because they have been reliably used to study PTHR signaling and trafficking (Ferrandon *et al.*, 2009; Feinstein *et al.*, 2011). myc-PTHR bound to the full-length SNX27 (Figure 1E). In contrast, no detectable levels of PTHR were observed after its coimmunoprecipitation with GFP alone (control). PTHR binding was reduced upon mutation of the SNX27 PDZ domain (H114A) and completely abolished after removal of the entire PDZ protein-interaction module (ΔPDZ; Figure 1E).

We next reasoned that if SNX27–PTHR interaction is physiologically important, then the two proteins should also colocalize to the same intracellular compartments in intact cells. Here PTH-PTHR ligand receptor complexes were visualized using N-terminally GFP-tagged (exon 2) PTHR ($^{GFP\text{-}N}$–PTHR) in combination with a fluorescent tetramethylrhodamine (TMR)-labeled PTH(1-34) analogue (herein PTH^{-TMR}), which has been routinely used as a probe to monitor PTH internalization and trafficking (Ferrandon *et al.*, 2009; Qiu *et al.*, 2010; Feinstein *et al.*, 2011). When PTH^{-TMR} was administered to a $^{GFP\text{-}N}$–PTHR-HEK293 cell clone at steady state (0; 4°C, 10 min), PTH-PTHR complexes localized predominantly at the cell surface, with little to no fluorescence overlap with endogenous SNX27, which was restricted to a population of intracellular vesicles (Figure 1F). These vesicles were identified as endosomes by their colocalization with the early endosome marker early endosome antigen-1 (EEA1), small GTPase Rab5, and phosphatidylinositol 3-phosphate lipid sensor Fab1p/YOTB/Vac1/EEA1 (FYVE; Supplemental Figures S1 and S2). Colocalization between SNX27 and $^{GFP\text{-}N}$–PTHR on endosomes was evident within 5 min of PTH stimulation, with peak fluorescence overlap observed at 15–30 min poststimulation (Figure 1F). At 60 min poststimulation, a subset of SNX27-bearing endosomes overlapped, albeit partially, with $^{GFP\text{-}N}$–PTHR at a perinuclear compartment. This

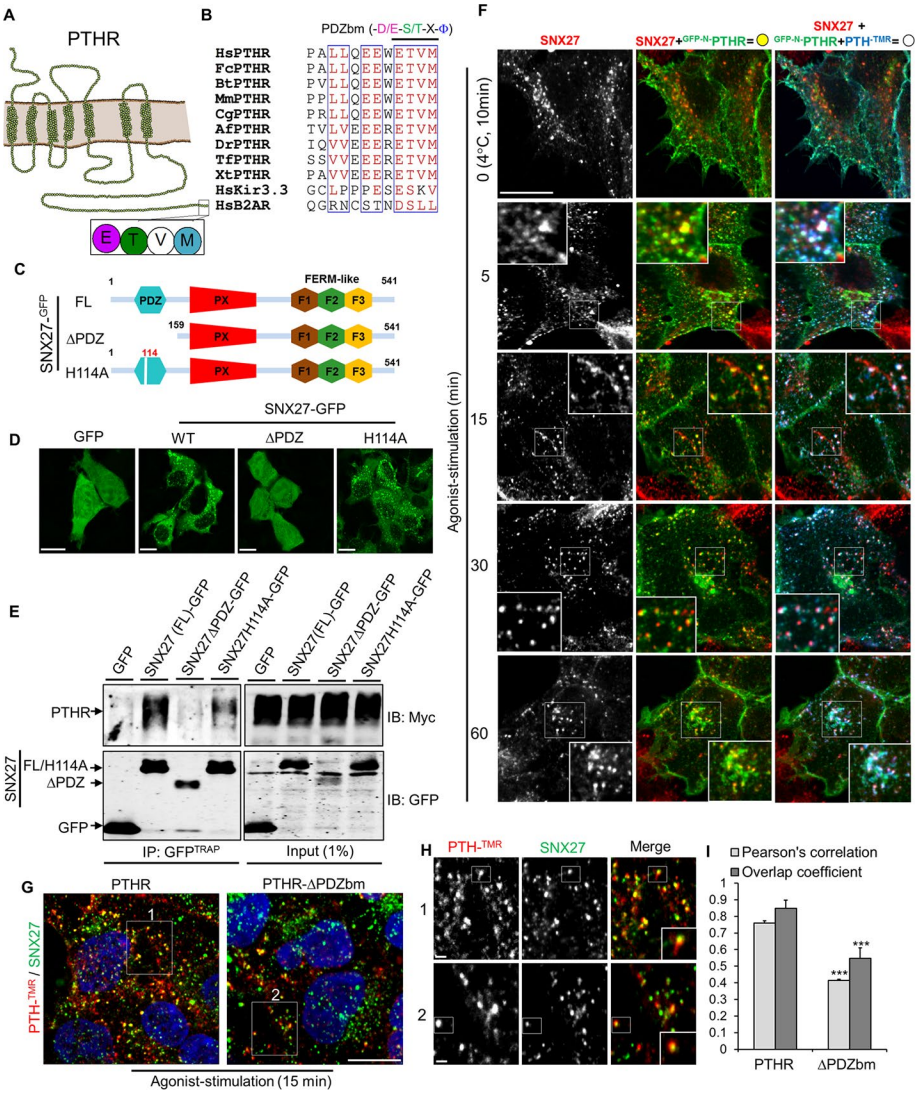

FIGURE 1: SNX27 interacts with internalized PTHR after activation. (A) Schematic drawing of PTHR, highlighting the PDZbm at the intracellular C-terminus. (B) Sequence conservation of the PDZbms of PTHR between species, together with published PDZbms of known SNX27-interacting partners β2AR and Kir3.3, using Jalview 2. (C, D) Schematic illustration and expression of C-terminally GFP-tagged SNX27 full-length (FL), PDZ truncation (ΔPDZ), and H114A mutant proteins in HEK293 cells. Bar, 10 μm. (E) Coimmunoprecipitation of HEK293 stably expressing ^{myc}–PTHR, with transient transfection of GFP, SNX27(FL)$^{–GFP}$, SNX27ΔPDZ$^{–GFP}$, or SNX27H114A$^{–GFP}$. Blots are representative of three independent experiments. (F) Agonist and time-dependent colocalization of $^{GFP\text{-}N–}$PTHR, PTH$^{–TMR}$, and endogenous SNX27 in HEK293 cells. Bar, 10 μm. (G–I) Comparative colocalization analysis of internalized PTH$^{–TMR}$ and SNX27 on endosomes in stable HEK293 cells expressing PTHR or PTHR ΔPDZbm at 15 min poststimulation. Bar, 10 μm. Inset, magnified boxed region. Bar, 1 μm. ***$p < 0.001$.

To explore further the spatiotemporal relationship between PTHR and SNX27 during agonist stimulation, we next coexpressed SNX27-mCherry and $^{GFP\text{-}N–}$PTHR in HEK293 cells and followed their response to PTH(1-34) by time-lapse confocal microscopy. When stimulated with agonist (100 nM PTH for 15 min), $^{GFP\text{-}N–}$PTHR was internalized into endosomes that colocalized with SNX27$^{–mCherry}$ and moved coordinately over time (Figure 2, A–D, and Supplemental Video S1). Of interest, PTHR internalization was observed most conspicuously at peripheral membrane ruffles in response to PTH and coincided with the colocalization of SNX27 with PTHR-bearing endosomes (Figure 2, E–G, and Supplemental Video S2). Although they occupy the same endosomes, SNX27 and PTHR signals were not completely superimposed immediately after PTH stimulation but instead spatially segregated along the outer limiting membrane, as confirmed by circumferential line-scan analysis (Figure 2B). At later time points, however (i.e., ~75 s after PTH stimulation), SNX27 and PTHR converged at common tubular protrusions emanating from the endosome surface (Figure 2, F and G). These protrusions were decorated with the recycling endosome marker Rab4b (Supplemental Figure S1) and were strikingly reminiscent of the retromer recycling tubules previously described for β2AR (Temkin *et al.*, 2011). Taken together, these data indicate that PTHR forms a complex with SNX27 via its PDZ-domain, which requires both the PTH-induced internalization of PTHR and an intact PTHR PDZbm for SNX27–PTHR association on endosomes.

SNX27 links PTHR to the retromer complex

To define the precise step(s) in the PTHR sorting and/or delivery cascade in which SNX27 operates, we further mapped its intracellular trafficking itinerary in relation to established components of the PTHR endocytic machinery. Because SNX27 (Temkin *et al.*, 2011) and PTHR (Feinstein *et al.*, 2011) have been independently shown to traffic along retromer-associated recycling pathway(s), we first assessed for colocalization between SNX27–PTHR and retromer after PTH stimulation. We observed extensive colocalization between SNX27 (SNX27$^{–GFP}$), PTHR (as monitored by PTH$^{–TMR}$), and retromer (here using antibodies against endogenous VPS35; Arighi *et al.*, 2004) on endosomes 15 min after PTH stimulation (Figure 3A). This close overlap was verified by measuring the fluorescence intensity peaks between respective image channels by correlative line-scan analyses (Figure 3B). SNX27–retromer association appeared independent of the PTHR endocytosis adaptor β-arrestin ($^{GFP–}$β-arrestin), whose fluorescence overlap with SNX27 (here SNX27$^{–mCherry}$) was found to decrease over time,

organelle was identified as the Golgi by immunostaining with the Golgi-resident marker TGN38 (Supplemental Figure S2). Of importance, similar colocalization with SNX27 was observed when PTH$^{–TMR}$ alone was used to monitor PTHR trafficking in a HEK293 cell clone stably expressing untagged PTHR (Supplemental Figure S3), confirming that the GFP tag did not influence subcellular trafficking of the receptor. On the other hand, removal of the PTHR-PDZ–binding motif (ΔPDZbm) significantly reduced colocalization between PTHR and SNX27 at 15 min post-PTH stimulation (Figure 1, G and I) as determined by Pearson's r (PTHR, $r = 0.759 \pm 0.02$, vs. PTHR-ΔPDZbm, $r = 0.415 \pm 0.06$), indicating that the C-terminal PDZbm is reciprocally required for association between PTHR and SNX27 on endosomes.

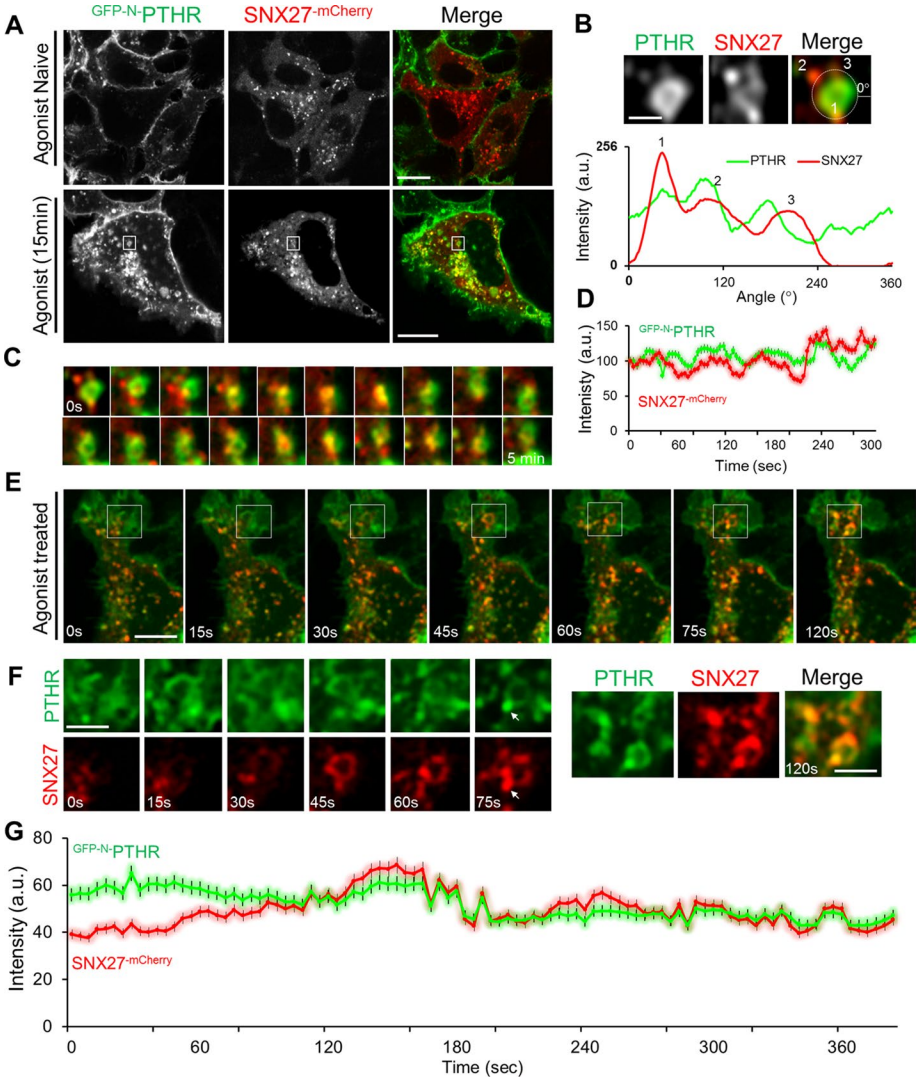

FIGURE 2: Spatiotemporal interaction of PTHR with SNX27 after endocytosis. (A) Time-lapse confocal microscopy of live HEK293 cells stably expressing $^{GFP\text{-}N}$–PTHR and SNX27$^{-mCherry}$. Interaction between $^{GFP\text{-}N}$–PTHR and SNX27$^{-mCherry}$ is shown at both the basal state (agonist naive) and 15 min poststimulation with 100 nM PTH(1-34). Bar, 10 μm. (B) Inset from A showing the localization and circumferential line-scan analysis of SNX27$^{-mCherry}$ to PTHR-positive endosomal microdomains, starting at 0°. Bar, 1 μm. (C, D) Time-lapse dynamics of HEK293 cells stably expressing $^{GFP\text{-}N}$–PTHR and SNX27$^{-mCherry}$ after stimulation with 100 nM PTH(1-34) across 5 min (C) and intensity plot over 300 s (D). (E, F) Mobilization of $^{GFP\text{-}N}$–PTHR and SNX27$^{-mCherry}$ to endosomes after stimulation with 100 nM PTH(1-34) across 120 s. Bar, 1 μm. (F) Inset from boxed region showing the recruitment of SNX27$^{-mCherry}$ to tubular endosomal protrusions occupied by $^{GFP\text{-}N}$–PTHR (arrow). Bar, 1 μm. (G) Fluorescence intensity tracking of colocalization between $^{GFP\text{-}N}$–PTHR and SNX27$^{-mCherry}$ across 360 s after agonist stimulation.

whereas SNX27-retromer association remained stable throughout the stimulation period (Figure 3, C and D), consistent with the view that they form part of the same endocytic recycling complex (Steinberg *et al.*, 2013; Gallon *et al.*, 2014).

The PDZ-dependent SNX27–PTHR interaction, together with the striking colocalization observed between these binding partners and retromer, suggested that SNX27 serves as a physical platform to scaffold PTHR to the retromer complex. To assess this, we used isothermal titration calorimetry (ITC) to measure the binding of the putative C-terminal PTHR PDZbm to the SNX27 PDZ domain. We used a synthetic peptide representing the C-terminal eight residues of the PTHR (^{586}QEEWETVM^{593}). In comparison to the type 1 PDZbms of GLUT1 and Kir3.3, two cargoes trafficked by the SNX27–retromer pathway (Steinberg *et al.*, 2013), the PTHR PDZbm bound more tightly to the SNX27 PDZ domain ($K_d \approx 6.3$ μM, compared with 17 and 154 μM for Kir3.3 and GLUT1, respectively; Figure 4A). Of importance, this binding is allosterically enhanced upon association with VPS26A ($K_d \approx 2.2$ μM; enthalpic increase from $\Delta H \approx -13.7$ to −19.7 kcal/mol), confirming that the SNX27–retromer complex physiologically forms a trimeric complex with PTHR. This allosteric enhancement is similar to what we previously observed for Kir3.3 (Gallon *et al.*, 2014). By comparison, the PDZ binding–defective mutant of SNX27 (H114A) showed a dramatically reduced binding signal, as expected.

To investigate PTHR recognition at the atomic level, we next determined the crystal structure of the SNX27 PDZ domain bound to a PTHR peptide at ultrahigh resolution (0.95 Å; (Figure 4B and Table 1). The final model contains residues 40–135 for the SNX27 PDZ domain and 587–593 for the PTHR peptide (EEWETVM). Using the common nomenclature for PDZbm sequences, this corresponds to residues –6 to 0. High-quality electron density maps demonstrate that the PDZbm of PTHR binds in a similar orientation as in the previously published SNX27 PDZ–Kir3.3 complex (Balana *et al.*, 2011). The PTHR peptide forms an antiparallel β-strand interaction with β6 in the SNX27 PDZ domain. Two glutamic acid side chains (Glu^{-5} and Glu^{-3}) associate with a basic patch on the SNX27 surface, in particular forming an electrostatic interaction that encompasses the conserved Arg^{58} side chain of SNX27. This interaction could explain both the relatively high affinity of this peptide (and the similar Kir3.3; Gallon *et al.*, 2014)) for SNX27 and the highly favorable enthalpy of association measured by ITC (Figure 4B). The Glu^{-6} and Gln^{-7} residues were not well ordered in our crystal, suggesting that these amino acids are not directly implicated in SNX27 recognition. In detail (Figure 4C), our structure confirms that the C-terminal PDZ triplet TVM is crucial for the interaction. The terminal carboxyl group of Met^{0} establishes an array of hydrogen bonds with the backbone of the conserved GYGF residue stretch in SNX27, whereas Thr^{-2} forms a hydrogen bond with SNX27 His^{114}, explaining the requirement for serine or threonine at this position of the motif. In addition to intermolecular β-sheet main-chain contacts, PDZ recognition extends upstream of the canonical type I PDZ triplet and is mediated mainly by the two Glu^{-3} and Glu^{-5} residues. Glu^{-3} is embraced between SNX27 Asn^{56} and Arg^{58}, and Glu^{-5} similarly forms a salt bridge with Arg^{58}. This network of interactions cooperatively stabilizes the PTHR peptide in the PDZ cavity, burying a surface area of 470 Å^2 (PDBePISA server, www.ebi.ac.uk), and provides a basis for strong and specific association (Figure 4C). The Asn^{56} and

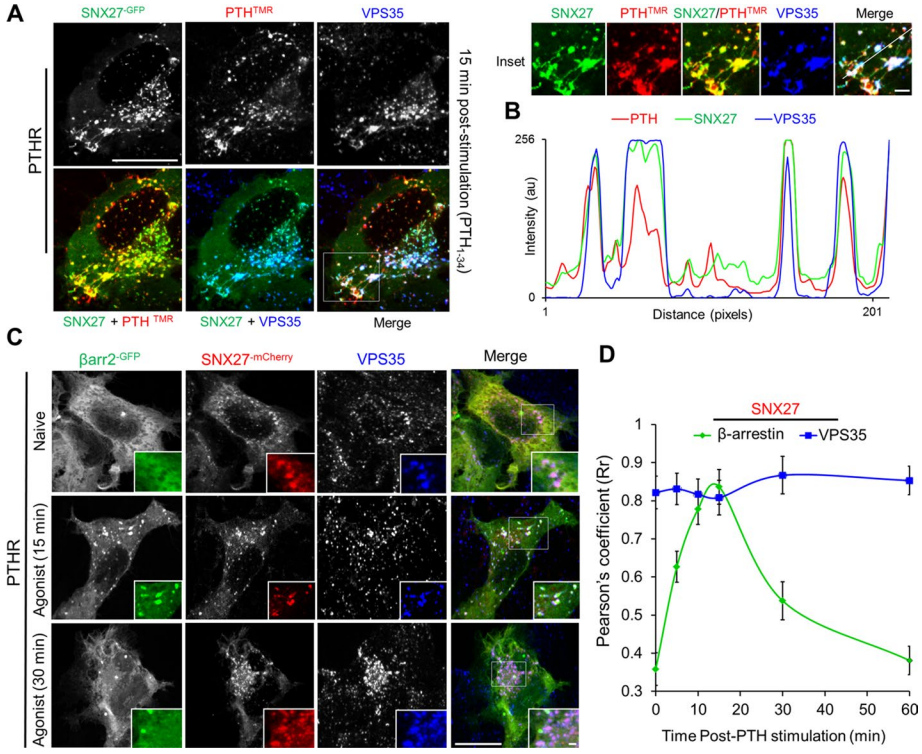

FIGURE 3: PTHR is transported in SNX27-retromer–decorated endosomal tubules. (A) Immunofluorescence staining of HEK293 cells stably expressing PTHR stimulated with PTH^{-TMR} for 15 min. Bar, 10 μm. Insets, colocalization of SNX27(FL)$^{-GFP}$, PTH^{-TMR}, and VPS35. Bar, 1 μm. (B) Correlative line-scan analyses of SNX27(FL)$^{-GFP}$, VPS35, and PTH^{-TMR} as shown in the merged inset in A. (C) HEK293 cells stably expressing PTHR were transiently cotransfected with β-arrestin2^{-GFP} and SNX27$^{-mCherry}$. Images show the recruitment of β-arrestin2^{-GFP} with SNX27$^{-mCherry}$ and VPS35 at 15 and 30 min poststimulation with 100 nM PTH(1-34). Bar, 10 μm. (D) Colocalization analysis of SNX27$^{-mCherry}$ with β-arrestin2^{-GFP} or VPS35 across 60 min. Values are mean ± SEM and are representative of three independent experiments.

Arg^{58} of SNX27 are conserved across species, as is the GYGF stretch that mediates binding to all PDZbm triplets (Ye and Zhang, 2013; Figure 4D). To confirm the structural basis of SNX27 binding to the PTHR, we mutated the PTHR sequence by either adding an Ala to the C-terminus or altering the Glu^{-3} side chain to Ala. Both alterations abolished binding to the PTHR peptides, according to ITC (Figure 4A). Taken together, these data confirm that PTHR binds directly to the SNX27 PDZ domain and that this interaction site is located close to the VPS26-binding surface of SNX27 (Figure 4E) and is allosterically coupled to SNX27–VPS26 association, as for Glut1 and Kir3.3 (Gallon *et al.*, 2014).

Depletion of SNX27–retromer causes sustained PTHR signaling

Because termination of cAMP generation from endosomal PTHR requires retromer (Feinstein *et al.*, 2011) and the results described so far indicate that SNX27 is the molecular adaptor that directs PTHR to retromer, we next asked whether SNX27 also functions to restrict cAMP signaling initiated by the receptor. For this, we used plasmid-based short hairpin RNAs (shRNAs) against SNX27 and VPS35 to deplete SNX27 and retromer expression in PTHR-expressing HEK293 cells and assessed the effects on PTHR-evoked cAMP signaling by examining the phosphorylation of several downstream second messenger pathways, including CREB, AKT, and MAPK (pERK1/2). Transfection and knockdown (KD) efficiencies were monitored by visualizing the percentage of cells expressing the GFP-reporter (~80%) and immunoblotting for SNX27 and VPS35 expression. Although not completely depleted, SNX27 and VPS35 levels were reduced by ~60 and ~80% respectively, compared with the nontargeting (control) shRNA (Figure 5, A and B). As seen previously (Feinstein *et al.*, 2011), we found that depletion of retromer resulted in augmented PTH-induced signaling, and, consistent with PTHR signaling operating through SNX27–retromer, knockdown of SNX27 had a similar effect. In particular, we found that the levels of phosphorylated CREB (pCREB) and pAKT were markedly elevated, whereas ERK1/2 phosphorylation was only modestly, although reproducibly, increased above control levels in SNX27 and VPS35 KD cells (Figure 5C). Of importance, exaggerated PTH signaling was most conspicuous within the 5- to 30-min window immediately after PTH stimulation, a period that coincided with formation of the SNX27/retromer transport tubules (Figure 3A and Supplemental Figure S4). These data indicate that, like retromer, SNX27 functions to restrict cAMP-evoked PTHR signaling at the endosome.

Two possible explanations might account for elevated PTH signaling in SNX27- and retromer-depleted cells: 1) increased PTHR expression at the cell surface (e.g., increased receptor synthesis or processing to the cell surface and/or altered constitutive trafficking) or 2) delayed termination of noncanonical PTHR signaling from endosomes. To distinguish these possibilities, we first examined the cell surface levels of PTHR in SNX27 and retromer KD cells using PTH^{-TMR} as a probe. Intriguingly, under resting conditions (i.e., temperature block 4°C, 10 min), we found that depletion of either SNX27 or VPS35 protein led to a reduction in PTH-PTHR surface levels (up to ~50% as quantified by PTH^{-TMR} intensity) compared with cells expressing nontargeting control shRNA (Figure 5, D and E). Thus the elevated PTHR signaling observed in SNX27- or retromer-depleted cells did not originate from enhanced levels of receptor at the cell surface.

We next checked whether loss of either SNX27 or retromer reroutes PTH-PTHR trafficking to a distinct endocytic compartment by monitoring the fate of internalized PTH^{-TMR} over various time points (up to 120 min) after PTH stimulation and washout in SNX27 and retromer-depleted cells in reference to the early endosome marker EEA-1. In PTH-stimulated PTHR-HEK293 cells expressing the nontargeting shRNA (unpublished data) or neighboring cells lacking expression of the SNX27 shRNA GFP reporter, PTH-PTHR consistently internalized into EEA-1–positive early endosomes at 5 min poststimulation (Figure 5, F and G) before entering VPS35-positive endosomes (typically within 10–30 min), with PTH^{-TMR} signal dissipating by 60–120 min poststimulation/washout, a period that coincided with repopulation of the receptor back to the PM (unpublished data). In comparison, whereas the low cell surface levels of PTH-PTHR precluded the ability to accurately track internalized PTH^{-TMR} in SNX27 and retromer KD cells (Figure 5, D and F) at time points immediately after administration of the PTH analogue (5–30 min), we did, however, observe PTH^{-TMR} signal in vesicular clusters at the perinuclear

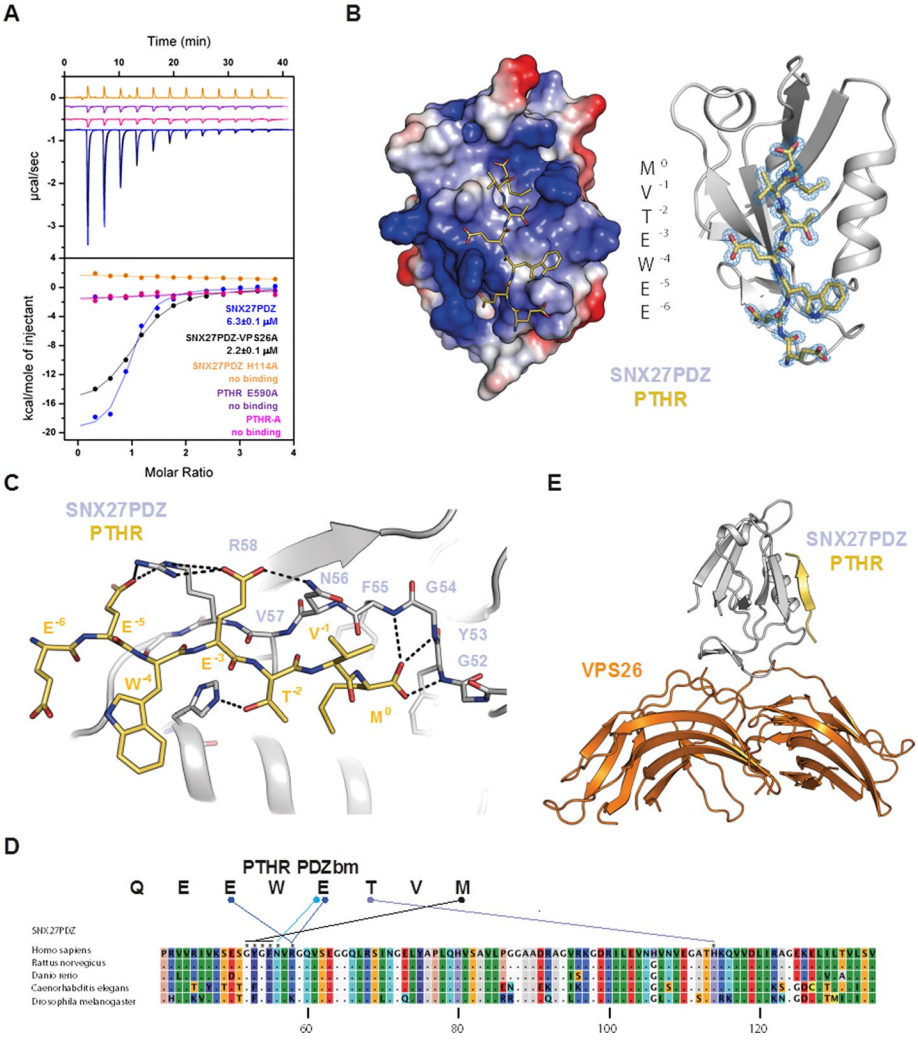

FIGURE 4: Structure of the SNX27 PDZ domain bound to the PTHR PDZ-binding motif. (A) The PTHR PDZbm peptide binds directly to the SNX27 PDZ domain in vitro (blue), and prior engagement by VPS26A facilitates this binding (black). Top, raw ITC data; bottom, integrated normalized data and calculated K_d values with SDs over three experiments. The SNX27 H114A mutation is shown as a negative control (orange). PTHR mutant peptides PTHR-E590A (purple) and PTHR-A (pink) fail to bind the SNX27 PDZ domain. (B) Electrostatic and ribbon representations of the SNX27 PDZ domain (gray) bound to PTHR peptide (yellow sticks) crystal structure. The PTHR peptide PDZbm sequence is displayed in the middle, and its refined $2F_o - F_c$ electron density contoured at 2σ is shown in blue. (C) Detailed view of the interaction surface between the SNX27 PDZ-binding cavity (gray) and PTHR (yellow). Critical contacts between residues governing the interaction are displayed as black dashed lines. (D) Alignment of amino acid sequences of SNX27 PDZ domains from various species and residues involved in binding to PTHR. Matching residues with the human sequence are depicted as dots. Alignment was generated using CLC BIO software. (E) Overlay of the SNX27 PDZ-VPS26A complex (PDB code 4P2A) with the SNX27 PDZ-PTHR complex (this study) structures highlights the different binding interfaces of both partners to SNX27. The SNX27 PDZ domain is shown in gray, VPS26 (VPS26A) in orange, and the PTHR peptide in yellow.

region of SNX27 and retromer KD cells at later time points (>60 min). These accumulated and were most conspicuous 120 min after PTH stimulation (Figure 5, F and H). These perinuclear clusters were distinct from early endosomes, as they lacked EEA-1 and were rarely observed in neighboring nontransfected or nontargeting shRNA control cells but were frequent in cells depleted of either SNX27 or VPS35 (Figure 5, F and H), implying that this was a general phenomenon upon disruption of the SNX27–retromer machinery. To reveal the nature of these PTH^{-TMR}-containing compartments, we performed immunostaining against various subcellular markers, including the lysosomal integral membrane protein (LAMP-1; Figure 5H), which identified this population of perinuclear vesicles as lysosomes. These data imply that down-regulation of SNX27 and retromer expression reduces PTHR surface levels, leads to an increase in sustained endosomal signaling, and stalls the entry of PTH into degradative lysosomes.

OBs lacking SNX27 display overactive PTH signaling and impaired mineralization activity in vitro

To confirm whether the observed disturbances in PTHR signaling in SNX27-retromer–depleted HEK293 cells translated physiologically, we further assessed the integrity of PTHR signaling in OBs (which natively express PTHR) isolated from SNX27-deficient (*SNX27*$^{-/-}$) mice (Cai *et al.*, 2011). First, we checked the functional consequence of SNX27 ablation on PTH-induced cAMP accumulation across a range of PTH concentrations. We observed a significant elevation in PTH-induced cAMP accumulation in OBs derived from bone marrow mesenchymal stem cells (BMSCs) from *SNX27*$^{-/-}$ mice compared with those from wild-type (WT) littermates (Figure 6A). We then probed cAMP-associated secondary messenger signaling pathways including pCREB, pAKT, and MAPK (pERK1/2), and found again that they were significantly increased in the early phase (5–30 min) of PTH stimulation (Figure 6, B–D) despite reduced cell surface PTH-PTHR levels (Supplemental Figure S5). Because PTHR also operates through the paracrine/autocrine ligand PTHrP in OBs (Miao *et al.*, 2005), we also checked whether SNX27 deficiency altered PTHrP-induced PTHR signaling. In this instance, PTHrP(1-141) stimulation induced elevated CREB and ATK phosphorylation profiles (most evident between the 5- and 30- min time points) in OBs derived from *SNX27*$^{-/-}$ mice compared with WT controls (Figure 6B). Intriguingly, we noted that the intensity of CREB phosphorylation was consistently more pronounced in OBs stimulated with PTHrP than in those exposed to PTH over the 90-min stimulation period (Figure 6C), possibly reflecting structural differences between PTHrP(1-141) and PTH(1-34) peptides or distinctions in the activation/deactivation kinetics, as previously reported for these two ligand systems (Ferrandon *et al.*, 2009).

PTH signaling is critical to OB differentiation and bone anabolic function (Datta and Abou-Samra, 2009). Therefore, to study the cumulative effect of PTHR deregulation on the function of *SNX27*$^{-/-}$ OBs, we assessed their differentiation and bone formation activity in vitro. Whereas the number of alkaline phosphatase (ALP)–expressing OBs obtained from BMSC-derived bone cell populations was largely indistinguishable between WT and SNX27-knockout littermates

A. Data collection	
Wavelength (Å)	0.88560
Space group	P212121
Cell dimensions	
a, *b*, *c* (Å)	37.1, 48.6, 55.7
a, b, g (°)	90, 90, 90
Resolution (Å)	15.72–0.95 (0.97–0.95)
R_{merge}	0.102 (1.70)
R_{meas}	0.112 (1.84)
R_{pim}	0.046 (0.701)
$<I>/\sigma I$	11.7 (1.6)
Total number of reflections	840,387 (41,355)
Total number of unique reflections	64,036 (3111)
Completeness (%)	99.8 (100.0)
Multiplicity	13.1 (13.3)
Half-set correlation (CC1/2)	0.994 (0.601)
Wilson *B*-factor	9.3
B. Refinement	
Resolution (Å)	14.8–0.95 (0.97–0.95)
Number of reflections/R_{free}	63,961/3238 (2581/137)
R_{work}/R_{free}	0.143/0.145 (0.243/0.253)
Number of atoms	
Protein	1654
Solvent	185
Average *B*-factor (Å^2)	19.4
Root mean squared deviations	
Bond lengths (Å)	0.008
Bond angles (deg)	1.278

Highest-resolution shell is shown in parentheses.

TABLE 1: Summary of crystallographic structure determination statistics.

(Figure 6E), loss of SNX27 significantly reduced their capacity to form mineralized bone nodules in vitro when cultured in the presence of osteogenic media (Figure 6, E and F). This impairment in osteoblastic mineralizing function was not unique to BMSC-derived osteoblastic cells, as similar defects were observed in primary OBs isolated from calvarial bone (Figure 6G) and long-bone explants (unpublished data). To assess whether the reduced mineralizing capacity in *SNX27*$^{-/-}$ OBs reflected altered PTH signaling and impaired OB differentiation, we further analyzed the mRNA expression of PTH-responsive markers of OB differentiation in cultured BMSC-derived OBs. Of interest, we noted significant up-regulation in the mRNA expression of early OB differentiation marker ALP and osteogenic transcriptional factors *RUNX2*, osterix (*OSX*), and osteoclastogenic cytokine *RANKL* in OBs derived from *SNX27*$^{-/-}$ mice compared with cells from WT controls (Figure 6H). By comparison, markers characteristic of fully differentiated and mineralizing OBs, such as the matrix extracellular phosphoglycoprotein *(MEPE)* and phosphate-regulating neutral endopeptidase (*Phex*) were robustly down-regulated in *SNX27*$^{-/-}$ OBs compared with controls (Figure 6F), whereas the expression levels of retromer (VPS35) remained constant between WT and *SNX27*$^{-/-}$ OBs (Supplemental Figure S6). Taken together, these data imply that the absence of SNX27 leads to overactive endosomal PTHR signaling, failed terminal differentiation of OBs, and thus impaired mineralizing function.

Postnatal SNX27-knockout mice exhibit skeletal growth deficits and reduced bone mass

PTHR is a crucial regulator of postnatal bone development and remodeling. Because our studies identify PTHR as a novel SNX27-interacting cargo and a role for SNX27 in bone morphogenesis had not been ascribed, we further assessed the pathophysiological consequences of SNX27 ablation on the mouse skeleton. *SNX27*$^{-/-}$ mice die at 4 wk postpartum (Cai *et al.*, 2011). Skeletal examination of P5 *SNX27*$^{-/-}$ mice by whole-mount preparations and three-dimensional (3D) micro–computed tomographic (μCT) reconstruction revealed overall impairment in skeletal growth in *SNX27*$^{-/-}$ mice (Figure 7, A and B). Reflecting this, SNX27-deficient mice were macroscopically smaller and exhibited shortening of limbs and tails and smaller skull sizes that were of reduced bone density compared with their WT and heterozygous littermates. These developmental disturbances extended to long bones (femurs and tibias), forelimbs (humerus, ulna and radius), and spines of 4-wk *SNX2*$^{-/-}$ mice (Figure 7, C–F). Detailed longitudinal reconstruction and assessment of microarchitectural bone parameters of femora and tibia isolated from 4-wk-old, sex-matched littermates revealed that bone trabeculation within the metaphyseal regions was drastically reduced in *SNX27*$^{-/-}$ mice (Figure 8, A and C). In addition, severe cortical thinning was observed in cross-sectional views in long bones of *SNX27*$^{-/-}$ mice compared with their littermate controls (Figure 8B). These profound reductions in trabecular bone volume (BV/TV) and trabecular number (Tb.N.) and thickness (Tb.Th.) were also verified by histomorphometric analysis (Figure 8, D and E).

To distinguish whether the drastically reduced bone mass might result from enhanced bone resorption by osteoclasts or reduced bone formation by OBs, we analyzed the number of tartrate-resistant acid phosphatase (TRAP)–positive osteoclasts at the trabecular of *SNX27*$^{-/-}$ bones. We found that the osteoclast number per bone surface (OC.N/BS [mm]) was only marginally decreased in the bones of *SNX27*$^{-/-}$ mice compared with WT littermates (Figure 8, F and G). In comparison, histomorphometric assessment of the number of OBs occupying trabecular bone surfaces (OB.N) revealed that they were substantially reduced in the long bones of *SNX27*$^{-/-}$ mice (Figure 8, H and I). Reflecting this, the total deposition (OS/BS) and thickness (O.WI [mm]) of recently deposited unmineralized bone (osteoid) was equally reduced in *SNX27*$^{-/-}$ mice (Figure 8I). Therefore the decrease in bone mass in SNX27-deficient mice results from inadequate osteoblastic differentiation and bone formation and not enhanced bone resorption.

Finally, in addition to the observed microarchitectural changes in bone density, there was a conspicuous enlargement of the gap between the tibial and femoral diaphysis and epiphysis (Figure 8A). Histological assessment of long bones revealed that this cartilaginous expansion arose from postnatal delays in the formation of the secondary ossification center and epiphyseal growth plate in *SNX27*$^{-/-}$ mice (Figure 8, D and J). Tibial and femoral growth plates of *SNX27*$^{-/-}$ mice are ~50% longer than in WT (Figure 8K), as confirmed by immunohistochemistry for the chondrocytic marker type II collagen (Figure 8J). Despite these anomalies, the characteristic columnar cellular organization and proteoglycan levels (periodic acid-Schiff [PAS]

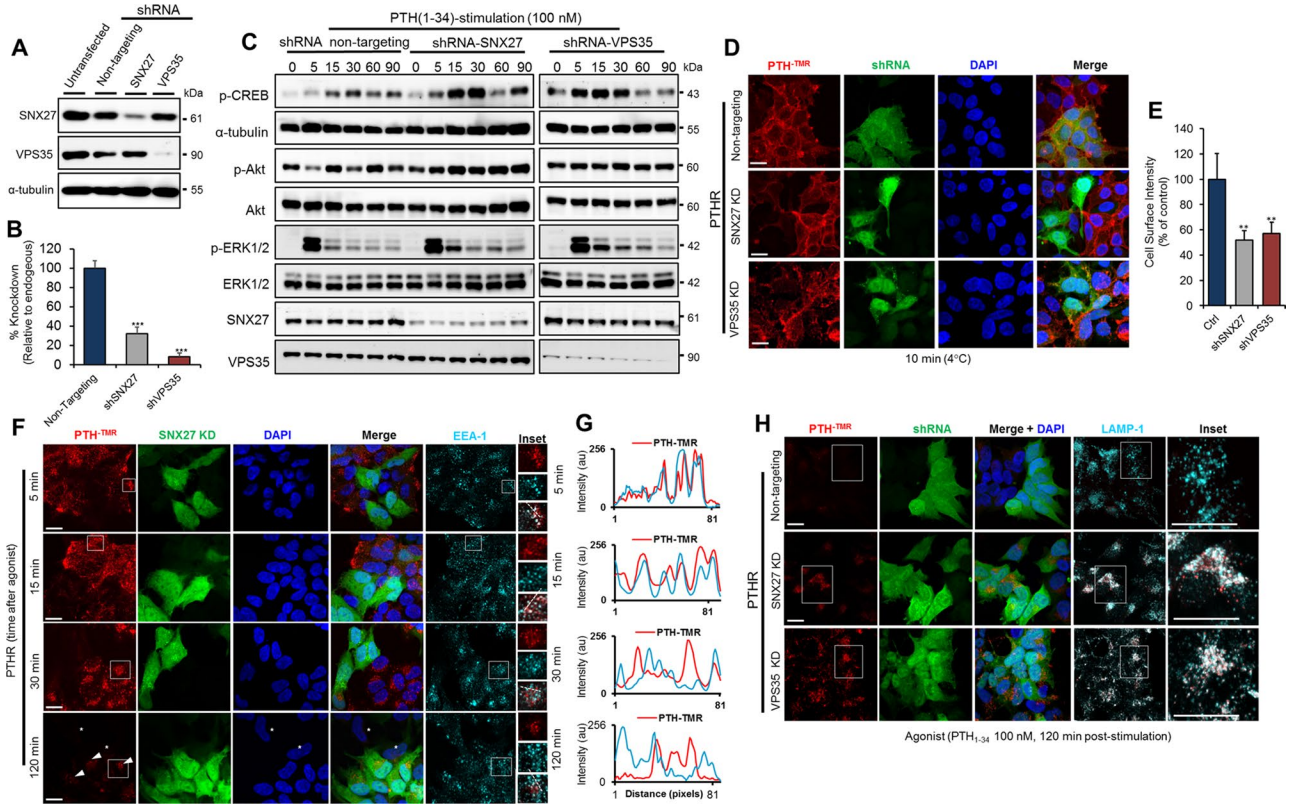

FIGURE 5: SNX27 and retromer coordinate the termination of intracellular signaling by PTHR. (A, B) Western blot and quantitation showing silencing efficiency in HEK293 stably expressing PTHR and nontargeting shRNA, shSNX27 (60%), or shVPS35 (80%). (C) HEK293 stably expressing PTHR and nontargeting shRNA, shSNX27, or shVPS35 were stimulated with 100 nM PTH(1-34) for 15 min, followed by a washout. Signaling pathways (CREB, AKT, ERK) were assessed by Western blotting. (D) Immunofluorescence staining of stable HEK293 shRNA-positive cells (GFP-positive) with 100 nM PTH^{-TMR} surface labeling. Bar, 10 μm. (E) Quantitation of cell surface intensity of PTH^{-TMR} as a percentage of nontargeting. Fifty cells were quantified per group. Values are mean ± SEM and are representative of three independent experiments. $^{**}p < 0.01$. (F) Immunofluorescence staining of shSNX27-positive cells (GFP-positive) with EEA1 after time-course stimulation of 100 nM PTH(1-34) (followed by washout after 15 min) and fixed at indicated time points. Bar, 10 μm. (G) Fluorescence intensity traces between PTH^{-TMR} and EEA1 across time-course stimulation as shown in F. (H) Immunofluorescence staining of shRNA-positive cells (GFP-positive) with LAMP-1 after 100 nM PTH^{-TMR} stimulation (followed by washout after 15 min) and fixed at 120 min. Bar, 10 μm.

and Safranin O staining) of the growth plate layers were generally well preserved. Viewed collectively, these data indicate that the maturation of the postnatal skeleton in SNX27-deficient mice is severely delayed due, at least in part, to growth plate abnormalities and reduced osteoblastic differentiation and bone formation.

DISCUSSION

Here we report multiple lines of evidence to indicate that SNX27 functions as an endosomal cargo adaptor for PTHR, a clinically important GPCR central to normal bone homeostasis and systemic calcium regulation. We show that SNX27 associates with endosomes bearing PTHR after agonist-induced internalization, where it binds directly to PTHR with high affinity and simultaneously scaffolds the receptor to the retromer complex. Recruitment of PTHR to SNX27-retromer–recycling tubules restricts PTH-evoked cAMP signaling, a prerequisite for PTHR signal regulation and function in OBs during postnatal bone growth and remodeling.

The spatiotemporal segregation of GPCR signaling in endosomes is now recognized as a key process in the cell's response to different stimuli (von Zastrow and Sorkin, 2007; Sorkin and von Zastrow, 2009). In the case of PTHR, it has been suggested that activation by PTH can promote sustained endosomal signaling but PTHrP cannot (Vilardaga *et al.*, 2014). Several reports have shown that the endosome also acts as the site for PTHR signaling desensitization after PKA-mediated intraluminal acidification and recruitment of select endocytic machineries (Feinstein *et al.*, 2011; Gidon *et al.*, 2014; Vilardaga *et al.*, 2014). Our work confirms the central role of retromer in terminating cAMP production by PTHR. However, until now, the molecular basis for this was incompletely understood. It was suggested that retromer likely controlled retrograde trafficking of PTHR to the TGN (Feinstein *et al.*, 2011) and might associate with PTHR via either the structural similarity of the VPS26 retromer subunit to β-arrestins (Shi *et al.*, 2006; Collins, 2008; Aubry *et al.*, 2009) or binding of an aromatic-containing FLN sequence to the retromer VPS35 subunit, although no direct interactions were shown (Feinstein *et al.*, 2011; Vilardaga *et al.*, 2014). Our results clearly show that SNX27 serves as an endosomal platform to integrate PTHR signal activation and retromer-mediated termination. We propose that SNX27 not only confers spatiotemporal control over endosomal PTHR signaling, but that it also directs PTHR to retromer for recycling back to the plasma membrane (possibly via the TGN), thus providing a mechanistic basis for SNX27/retromer–mediated signal attenuation (Figure 9).

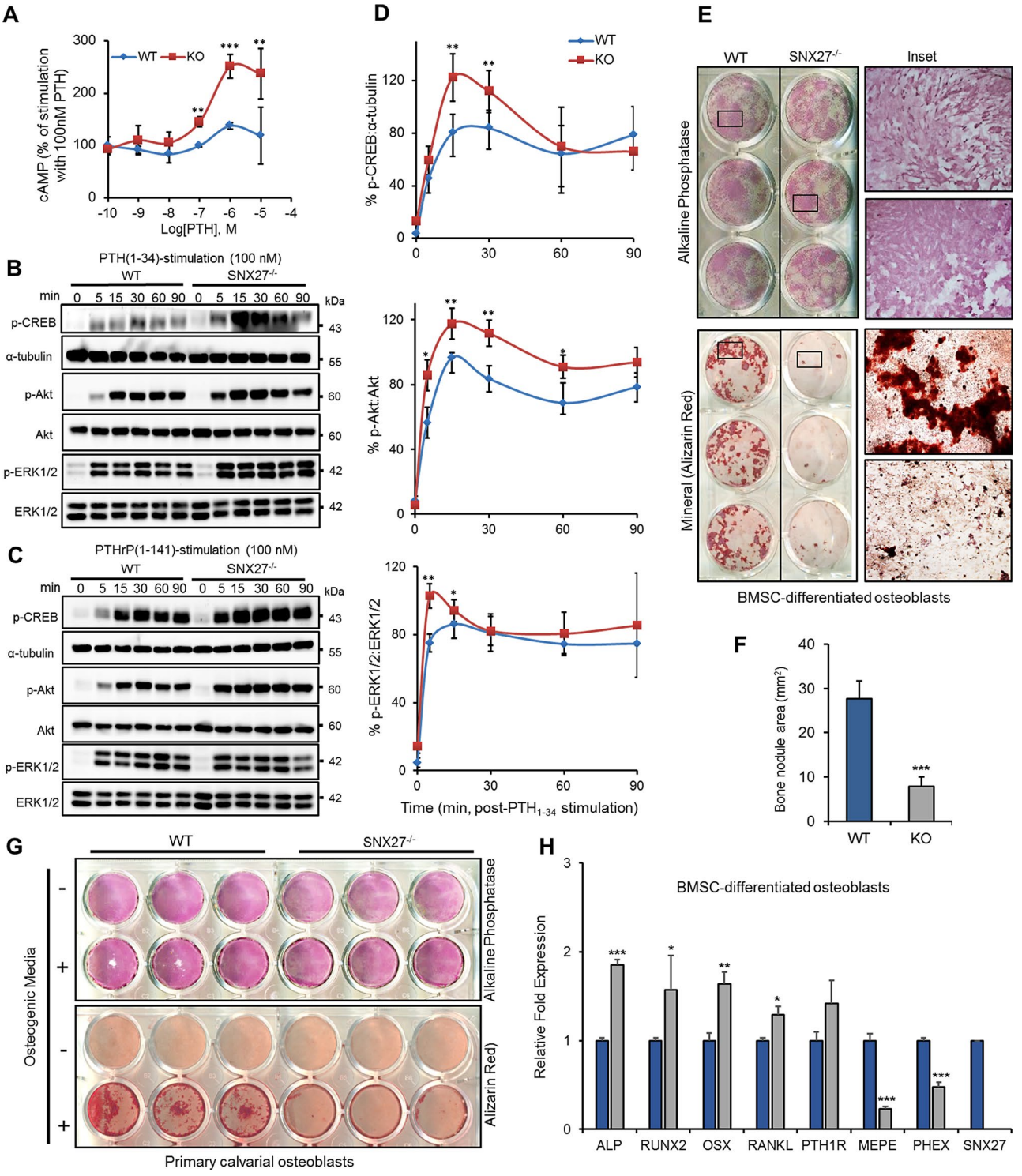

FIGURE 6: SNX27 is required for PTHR signal termination in OBs and OB differentiation. (A) Cyclic AMP assay performed on SNX27 WT and SNX27$^{-/-}$ OBs stimulated for 10 min with increasing concentrations of PTH(1-34). (B, C) SNX27 WT and SNX27$^{-/-}$ OBs were stimulated with 100 nM PTH(1-34) (B) or 100 nM PTHrP(1-141) (C), for 15 min, followed by a washout. Signaling pathways (CREB, AKT, ERK) were assessed through Western blotting. (D) Densitometry quantification of protein bands from SNX27 WT and SNX27$^{-/-}$ Western blots (B) were conducted using Photoshop 2014 and expressed as a percentage with respect to their respective control. (E) ALP and alizarin red staining (ARS) of SNX27 WT and SNX27$^{-/-}$ BMSC-derived OBs cultured in vitro under mineralizing conditions (50 μg/ml L-ascorbic acid, 2 mM β-glycerophosphate, 10^{-8} M dexamethasone) for 21 d. (F) Quantification of ARS-positive nodules per square millimeter using ImageJ. (G) Calvarial OBs isolated from SNX27 WT and SNX27$^{-/-}$ were cultured under mineralizing conditions (+) for 21 d and stained with ALP or ARS. (H) mRNA expression from BMSC-derived SNX27 WT and SNX27$^{-/-}$ OBs was analyzed through quantitative PCR, using HMBS as a reference gene. *$p < 0.05$, **$p < 0.01$, and ***$p < 0.001$.

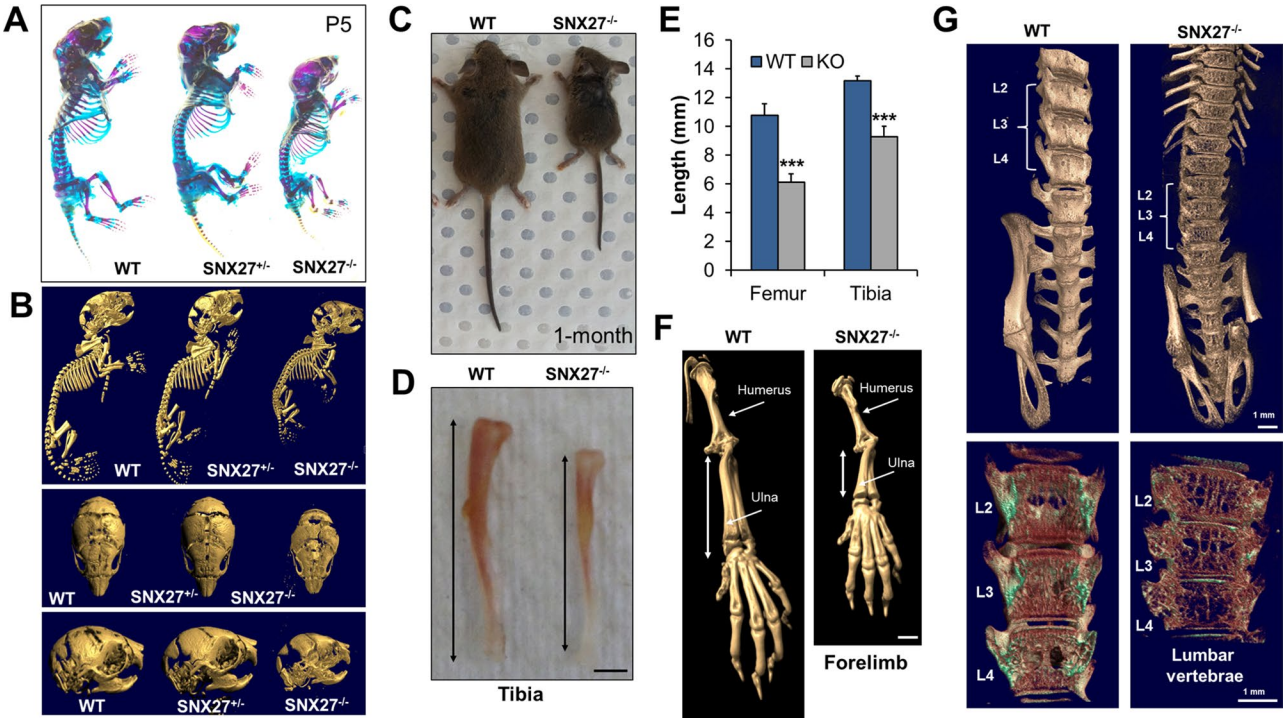

FIGURE 7: Skeletal overview of SNX27-knockout mice. (A) Whole-mount skeletal preparations stained for Alcian blue (cartilage) and Alizarin red (bone). (B) μCT analysis of SNX27-knockout mice (*SNX27*$^{-/-}$) compared with heterozygous (*SNX27*$^{+/-}$) and WT littermates at P5. Top and side 3D μCT reconstructions of the skull reveal reduced bone density of cranial sutures in *SNX27*$^{-/-}$ mice. (C, D) Gross anatomy of SNX27 WT and *SNX27*$^{-/-}$ mice at 4 wk of age. (E) Measurements of the lengths of femurs and tibias from WT and *SNX27*$^{-/-}$ mice. (F, G) μCT surface reconstructions of forelimbs and spine from WT and *SNX27*$^{-/-}$ mice. Insets, detailed view of L2–L4. Scale bar, 1 mm. Values are mean ± SEM from six mice per group. ***$p < 0.001$.

As with other SNX27-interacting cargo, for example, Kir3.3 (Balana *et al.*, 2011), our findings demonstrate that PTHR cargo recognition is achieved via its C-terminal PDZbm, which binds with high affinity to the N-terminal PDZ domain of SNX27. Of importance, the PDZ domain not only discriminates SNX27 from other SNX family members, but it also serves as an interaction module to simultaneously wire PTHR to the retromer core subunit VPS26. VPS26 binding additionally stabilizes and enhances the affinity of the SNX27 PDZ domain for the PTHR-PDZbm, a feature common to other SNX27-retromer–interacting cargo housing PDZbms (Gallon *et al.*, 2014). Similar to Kir3.3 (PESE; Balana *et al.*, 2011), the PTHR houses a four–amino acid stretch (EEWE) encoded immediately upstream of the canonical PDZbm triplet (TVM) that encompasses two acidic glutamate residues, at positions −3 and −5, that form a strong electrostatic interaction with the conserved Arg^{58} side chain of the SNX27 PDZ domain. Precisely how this linear amino acid stretch accounts for the preferential binding of affinity of the PTHR observed over other known SNX27 PDZbm-bearing cargo (Clairfeuille and Collins, unpublished data) forms the subject of our future studies.

Together with previous work describing a role for the retromer complex in endosomal PTHR trafficking (Feinstein *et al.*, 2011), our morphological and signaling analyses best support a function for SNX27 as a molecular adaptor for recruiting PTHR into retromer-decorated tubules for endosome-to–cell surface recycling. SNX27/retromer-mediated transport thus attenuates sustained endosome-associated PTHR signaling. This conclusion is supported by our evidence that genetic ablation of SNX27 leads to enhanced cAMP accumulation and subsequent overactivation of downstream signaling cascades upon PTHR stimulation, most evident at times that parallel receptor internalization into SNX27 and retromer-bearing endosomes in PTHR-expressing HEK293 cells. We further show that depletion of the SNX27 or retromer leads to a reduction in PTH-PTHR cell surface levels, presumably reflecting reduced recycling rates or mistrafficking of the receptor (e.g., into lysosomes) as observed for other SNX27 PDZbm-bearing cargoes (Steinberg *et al.*, 2013; Gallon *et al.*, 2014). In fact, during the course of this investigation, depletion of either SNX27 or retromer (VPS35) was independently shown to correlate with a 50% decrease in the rate of PTHR recycling at the cell surface following agonist stimulation (J. McGarvey and P.A. Friedman, personal communication).

Intriguingly, despite these reduced cell surface levels, PTH-induced PTHR signaling remains elevated upon SNX27 and retromer disruption. This implies that the levels of PTHR remaining on the cell surface are sufficient to elicit signal sensitization when ligands are added at saturating concentrations. It also implies that newly synthesized PTHR or compensatory retrieval mechanism(s) might help to maintain PTHR levels when SNX27–retromer expression becomes limited. For example, cytosolic NHERF proteins (NHERF1/2) contain PDZ module(s) that also bind to the PTHR PDZbm (Mahon *et al.*, 2002; Sneddon *et al.*, 2003) and have been reported to regulate the membrane retention, trafficking, and desensitization of PTHR (Wang *et al.*, 2007, 2008; Ardura *et al.*, 2011; Wheeler *et al.*, 2011). Of interest, mice lacking NHERF1 (Shenolikar *et al.*, 2002) and patients harboring NHERF1 mutations (Karim *et al.*, 2008) manifest bone abnormalities (osteopenia and osteomalacia; Weinman *et al.*, 2006; Liu *et al.*, 2012) that are attributed, in part, to overactivated PTH

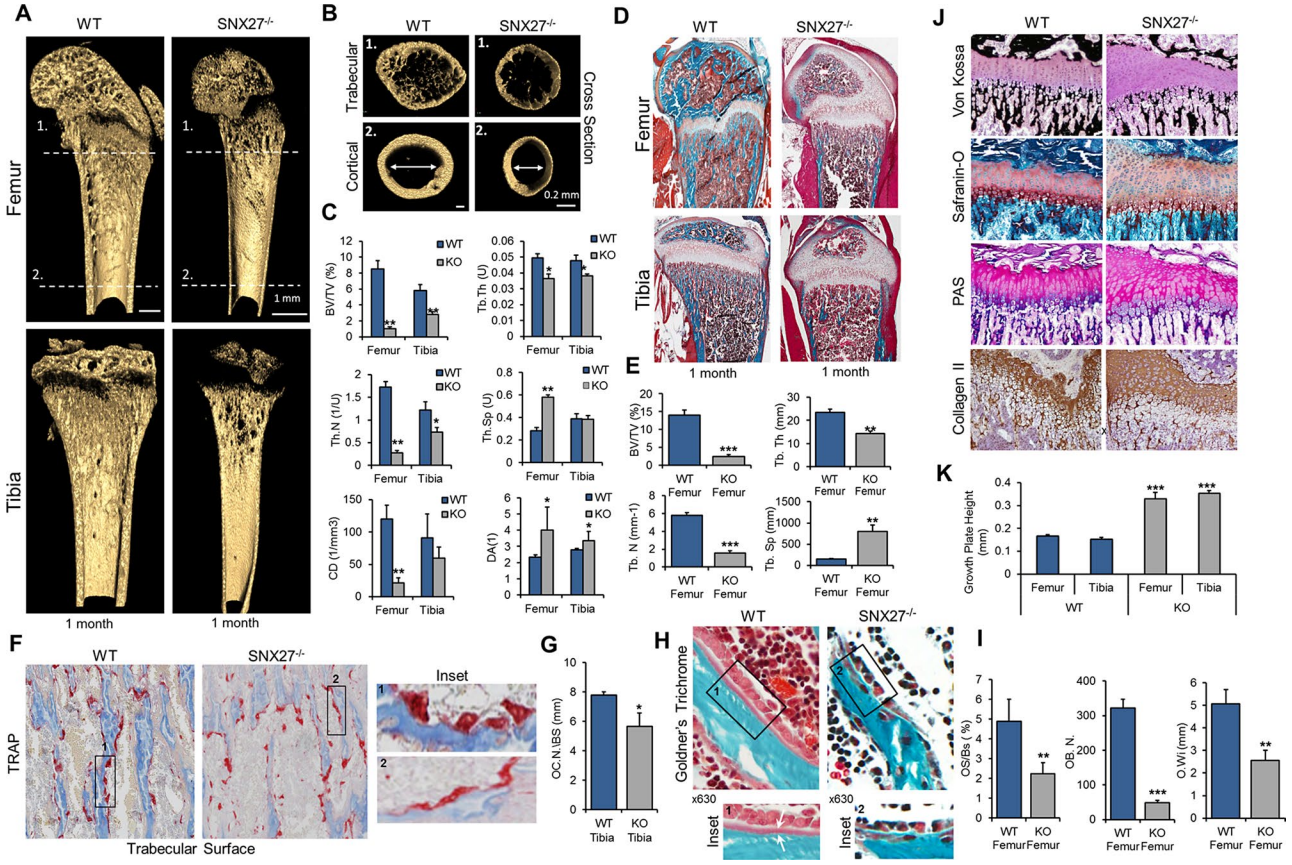

FIGURE 8: SNX27$^{-/-}$-knockout mice show profound bone abnormalities due to OB dysfunction. (A) Representative reconstructed μCT images of 1-mo-old SNX27 WT and SNX27$^{-/-}$ tibia and femur. Scale bar, 1 mm. (B) Representative cross-sectional planes of distal femoral metaphysis (1) and cortical bone (2) as indicated in A. Scale bar, 0.2 mm. (C) Changes in bone volume/tissue volume (BV/TV, %), trabecular thickness (Tb.Th, U), trabecular number (Tb.N, 1/U), trabecular separation (Th.Sp, U), connectivity density (CD, 1/mm^3), and degree of anisotropy (DA, 1) in SNX27$^{-/-}$ compared with WT. (D) Goldner's trichrome staining of longitudinal sections of femur (top) and tibia (bottom) in 1-mo-old SNX27 WT and SNX27$^{-/-}$ mice. (E) Histomorphometric analysis showing changes in BV/TV, Tb.Th, Tb.N, and Tb.Sp in SNX27$^{-/-}$ compared with WT. (F) TRAP staining in 1-mo-old SNX27 WT and SNX27$^{-/-}$ tibia. Insets, osteoclast morphology lining trabecular in vivo. (G) Histomorphometric analysis showing changes in osteoclast number per bone surface (OC.N/BS, mm) in SNX27 WT and SNX27$^{-/-}$ tibia. (H) Goldner's trichrome staining of trabecular in 1-mo-old SNX27 WT and SNX27$^{-/-}$. Insets, OB morphology in vivo and osteoid production (white arrows; 630×). (I) Histomorphometric analysis showing changes in osteoid per bone surface (OS/Bs, %), OB number (OB.N), and osteoid width (O.Wi, mm) in SNX27 WT and SNX27$^{-/-}$ tibia. (J) Von Kossa, Safranin O, and PAS stains and collagen type 2 immunohistochemistry of SNX27 WT and SNX27$^{-/-}$ epiphyseal growth plate of tibia (200×). (K) Changes in epiphyseal growth plate height (mm) in SNX27 WT and SNX27$^{-/-}$ tibia and femur. *$p < 0.05$, **$p < 0.01$, and ***$p < 0.001$.

signaling and impaired mineralization capacity in OBs (Liu *et al.*, 2012), in keeping with the skeletal deficits observed in *SNX27*$^{-/-}$ mice in our study. The precise interrelationship that exists between PTHR, NHERFs, and SNX27-retromer is unclear, but it appears that at least two PDZ-dependent modes of PTHR trafficking can operate in vertebrates to modulate cell surface levels—one regulated by NHERF1 (Ardura *et al.*, 2011) and the other presided over by SNX27, as shown in this study.

SNX27 disruption in humans (Damseh *et al.*, 2015) and mice (Cai *et al.*, 2011) manifests in severe growth and developmental disturbances (as shown here) and also correlates with net alterations in the expression of many critical neuronal proteins (Cai *et al.*, 2011; Wang *et al.*, 2013, 2014; Loo *et al.*, 2014). Although SNX27 is expressed in many tissues (including bone; Chan and Pavlos, unpublished data), studies characterizing the effect of its disruption have been largely restricted to its role in the impairment of neuronal function. Our finding that SNX27 deficiency leads to severe skeletal dysplasia extends the physiological importance of SNX27 to bone morphogenesis. Of interest, the skeletal dysmorphisms exhibited in SNX27-deficent mice bear some resemblance to those in humans (Schipani *et al.*, 1995, 1996) and mice (Karaplis *et al.*, 1994; Lanske *et al.*, 1999; Calvi *et al.*, 2001; Miao *et al.*, 2002) with disruptions in PTHR and associated G protein–dependent signaling pathways (Weinstein *et al.*, 2006; Wu *et al.*, 2011). On one hand, the reduced cortical bone density, increased cAMP accumulation, overactivation of associated secondary messenger signaling cascades (pCREB, pAKT, and pERK1/2), along with the unregulated transcriptional expression of PTH-response genes observed in both unstimulated OBs and total bone, phenocopies those observed in osteoblastic cells from mice bearing constitutively active mutations in the *PTHR* gene (Calvi *et al.*, 2001) and/or deletion of Gα_s (Wu *et al.*, 2011). On the other hand, the expansion of the cartilaginous growth plate (as opposed to its premature closure) clearly distinguish SNX27-deficient mice from those with disrupted PTHR signaling pathways alone (Calvi *et al.*, 2001;

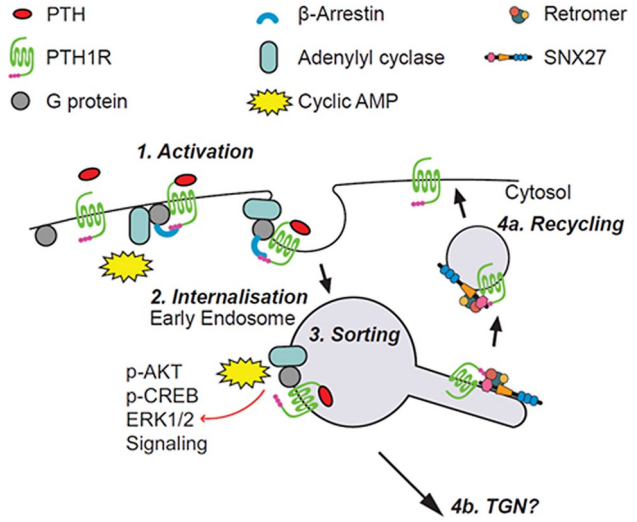

FIGURE 9: Hypothetical model of PTHR signaling and endosomal recycling after PTH-mediated receptor internalization. Activated PTHR is internalized into the early endosome and sorted for recycling back to the plasma membrane (possibly via the TGN) through direct interaction with SNX27–retromer. The illustration includes additional components (e.g., G proteins, adenylyl cyclases, etc.) based on contemporary models of the PTH-PTHR activation and internalization cycle (Ferrandon *et al.*, 2009; Feinstein *et al.*, 2011).

Kobayashi *et al.*, 2002; Miao *et al.*, 2002; Hirai *et al.*, 2011). Thus additional SNX27-signaling cargo must contribute to the bone phenotype. Indeed, the β2AR (Lauffer *et al.*, 2010; Temkin *et al.*, 2011), an established SNX27-binding GPCR, is functionally required for the anabolic action of PTHR on bone (Hanyu *et al.*, 2012). Receptors of other notable bone morphogens, including transforming growth factor β (TGFβ), BMPs, and Wnts, which intersect with PTHR and traffic via the retromer recycling pathway, may similarly add to the net bone phenotype (Qiu *et al.*, 2010; Harterink *et al.*, 2011; Yin *et al.*, 2013; Gleason *et al.*, 2014). Irrespective of the exact number of cargoes involved, our studies clearly demonstrate that PTHR is a physiologically important SNX27-PDZ cargo with central roles in bone growth and remodeling.

Unraveling the fundamental mechanisms governing PTHR signaling has been a focus of intensive experimental and pharmaceutical research (McCauley and Martin, 2012; Gardella and Vilardaga, 2015). The identification of new molecules, such as SNX27, that directly modulate PTHR signaling, trafficking, and function may open up new avenues for the development of more effective therapeutic agents that are applicable not only to disorders of bone metabolism like osteoporosis but also extend to wider metabolic syndromes.

MATERIALS AND METHODS

Antibodies, peptides, and constructs

We used the following materials from the respective suppliers: phospho-CREB, phospho-AKT, pan-AKT (Cell Signaling Technology, Danvers, MA); PTHR, phosphor-ERK1/2, VPS35 (Santa Cruz Biotechnology, Dallas, TX); total-ERK1/2 (Promega, Madison, WI); EEA1 and TGN38 (BD Biosciences, Franklin Lakes, NJ); SNX27, Lamp1 (Abcam, Cambridge, United Kingdom); anti-Myc (Merck Millipore, Darmstadt, Germany); anti-GFP (Enzo Life Sciences, Farmingdale, NY); collagen 2, α-tubulin, peroxidase-conjugated goat anti-mouse immunoglobulin (IgG), goat anti-rabbit IgG (Sigma-Aldrich, St. Louis, MO); Hoechst 33256 (Thermo Fisher Scientific, Waltham, MA). Human parathyroid hormone fragment PTH(1-34) was purchased from Sigma-Aldrich. A tetramethylrhodamine-labeled parathyroid hormone (PTH^{-TMR}) by which TMR was added to the ε-amino group of Lys^{13} of PTH(1-34) was synthesized from Genemed Synthesis (San Antonio, TX). PTHrP(1-141) was generously provided by T. J. (Jack) Martin (St Vincent's Institute of Medical Research, Melbourne, Australia). The PTHR synthetic peptides (QEEWETVM, QEEWATVM, and QEEWETVMA) used for ITC were from Genscript (Piscataway, NJ). Constructs were as follows: β-*srrestin2-GFP* (Addgene plasmid 35411); *SNX27(FL)*$^{-GFP}$, *SNX27ΔPDZ*$^{-GFP}$, and *SNX27(FL)*$^{-mCherry}$ (previously described in Loo *et al.*, 2014); and *SNX27H114A*$^{-GFP}$ (generated using QuikChange Site-Directed Mutagenesis Kit, Agilent Technologies, Santa Clara, CA). Stable knockdown HEK293 cell lines were generated using a lentivirus shRNA system (Thermo Fisher Scientific) with *pGIPZ shnontargeting* (RHS4346), *pGIPZ shSNX27* (V2LHS_237898), and *pGIPZ shVPS35* (V2LHS_156301). $^{GFP-}$Rab5 and $^{GFP-}$Rab4b constructs were previously described (Pavlos *et al.*, 2010). The mCherry-ML1N*2 plasmid as described by Li *et al.* (2013) was generated synthetically by Genscript and subcloned into pmCherryC1. The mCherry-2xFYVE construct was generated by subcloning $2xFYVE_{Hrs}$ from pEGFP-$2xFYVE_{Hrs}$ as detailed in Kerr *et al.* (2010). For construction of $^{GFP\text{-}N-}$*PTHR*, the N-terminus of the PTHR (residues 61–101) were replaced with the enhanced GFP sequence preceded by the linker Arg-Leu-Ile-Ser-Gly-Ser according to the methods described in Castro *et al.* (2005). Untagged *PTHR* and *PTHRΔPDZbm* were synthesized by Genscript. $^{myc-}$*PTHR* was generated by OriGene Technologies (Rockville, MD).

Animals

The generation of $SNX27^{-/-}$ mice was described previously (Cai *et al.*, 2011). This study was performed in strict accordance with the Animal Welfare Act 2002 (Western Australia) and requirements of the eighth (2013) edition of the Australian code for the care and use of animals for scientific purposes. All of the animals were handled according to institutional animal care protocols approved by the Animal Ethics Committee of the University of Western Australia (Approval No. RA/3/100/1399).

Cell culture and transfection

All cell culture products were purchased from Thermo Fisher Scientific. Primary mouse OBs were isolated from BMSCs and calvarial bone as described previously (Bakker and Klein-Nulend, 2012; Kular *et al.*, 2015) and cultured in complete α-MEM (10% fetal bovine serum [FBS], 100 U/ml penicillin, 100 U/ml streptomycin). HEK293 cells were cultured in complete DMEM-GlutaMAX (10% FBS, 2 mM L-glutamine, 100 U/ml penicillin, 100 U/ml streptomycin) and maintained in humidified conditions of 5% CO_2 at 37°C. Cells were transfected using Lipofectamine LTX (Thermo Fisher Scientific) according to the manufacturer's protocol. Stable cell lines were derived through antibiotic selection of neomycin/G418 at 500 μg/ml or puromycin at 2 μg/ml.

Immunoprecipitation

The respective plasmids were transfected into HEK293 cell line stably expressing $^{Myc-}$*PTHR*, using Lipofectamine LTX according to manufacturer's protocol. Cells were incubated for 48 h, followed by the addition of PTH(1-34) (100 nM) for 10 min. Cells were washed twice with ice-cold 1× phosphate-buffered saline (PBS) and lysed in nondenaturing extraction buffer (50 mM 4-(2-hydroxyethyl)-1-piperazineethanesulfonic acid [HEPES]–KOH, pH 7.2, 150 mM NaCl, 1 mM $MgCl_2$, 0.5 mM ethylene glycol tetraacetic acid, 1 mM phenylmethylsulfonyl fluoride [PMSF], 1× complete protease inhibitor [CPI], 0.1% Triton X-100) on ice. Cell lysate was homogenized and centrifuged at

15,000 rpm for 15 min at 4°C. Cleared lysate was incubated with GFP–Trap-A beads (ChromoTek, Planegg-Martinsried, Germany) overnight at 4°C. Beads were washed in washing buffer (20 mM HEPES-KOH, pH 7.2, 150 mM NaCl, 1 mM $MgCl_2$, 1 mM PMSF, 0.5% Triton X-100), boiled in 2× nondenaturing loading buffer, and resolved by SDS–PAGE (12%).

Immunofluorescence and time-lapse confocal microscopy

Stable transfected HEK293 cells were cultured on poly-L-lysine–coated glass coverslips for 48 h and serum starved for 1 h before stimulation with PTH(1-34) (100 nM) or PTH^{-TMR} (100 nM) over a time course of 0–120 min. After 15 min of stimulation, cells were washed twice with 1× PBS and replaced with complete medium. Cell surface PTH^{-TMR} fluorescence was detected by subjecting cells to an ice block (4°C for 10 min) and washing and then fixing them (4% paraformaldehyde [PFA]). Cells were then permeabilized with 0.1% Triton X-100 and/or 0.1% saponin and stained with indicated antibodies. Samples were mounted in ProLong Gold Antifade (Thermo Fisher Scientific) and imaged using a Nikon A1Si confocal microscope equipped with a 10× (dry) lens and a 60× (oil) lens (Nikon, Tokyo, Japan). Time-lapse confocal microscopy was performed under controlled atmospheric conditions (37°C and 5% CO_2/air) in a Tokai Hit (Fujinomiya, Japan) Stage Top incubator (INUG2E-TIZ) as previously described (Ng *et al.*, 2013).

Protein expression, purification, and crystallization

cDNAs of residues 9–327 of VPS26A (mouse) and 40–135 of SNX27 (rat) were cloned in a pMW172KanH6 plasmid downstream of a hexahistidine tag and in a pGEX4-T2, yielding an N-terminally GST-tagged protein. The QuikChange II Kit (Agilent Technologies) was used for site-directed mutagenesis. Proteins were expressed in *Escherichia coli* BL21 (DE3) strain overnight at 20°C and purified using affinity chromatography followed by gel filtration. VPS26A was purified on a nickel–nitrilotriacetic acid gravity column and eluted with 300 mM imidazole in buffer of 200 mM NaCl and 20 mM HEPES (pH 7). The SNX27 PDZ domain was purified on a glutathione–Sepharose gravity column and eluted after 3 h of thrombin cleavage in 200 mM NaCl/25 mM Tris (pH 8) buffer. Proteins were then gel filtered using a Sepharose S200 16/60 column attached to an AKTA system (GE Healthcare, Waukesha, WI). For crystallization, SNX27PDZ fractions were gel filtered into 20 mM Bis/Tris plus 30 mM NaCl (pH 6.5) buffer, pooled, and concentrated and then directly mixed together to a 2:1 M ratio of SNX27 PDZ domain to PTHR peptide, where the final SNX27 PDZ concentration was 25 mg/ml. Four 96-well crystallization hanging-drop screens were set up using a Mosquito Liquid Handling robot (TTP LabTech, Melbourn, United Kingdom) at 20°C. Optimized diffraction-quality crystals were obtained using the sitting drop vapor diffusion method and a buffer containing 0.1 M Bis/Tris (pH 5.5) and 2 M ammonium sulfate.

Data collection and structure determination

Data were collected at 100 K at beamline MX2 (Australian Synchrotron; Supplemental Table S1) and integrated and scaled with MOSFLM and SCALA. The structure was determined by molecular replacement using Phaser-MR (McCoy *et al.*, 2007) with the SNX27 PDZ domain crystal structure as an input (Protein Data Bank [PDB code] 3QDO). A model was built using COOT (Emsley *et al.*, 2010), followed by repeated refinement and model building with PHENIX. REFINE and COOT. All residues in the final model were built in accordance with Ramachandran statistics. The final structure was solved at 0.95-Å resolution and revealed electron density corresponding to all amino acids contained in the synthetic peptide but the Q^{-7} residue. All structural figures were generated using PyMOL (www.pymol.org).

Isothermal titration calorimetry

ITC experiments were performed on a MicroCal iTC200 instrument (Malvern, Malvern, United Kingdom) in 50 mM Tris (pH 8)/100 mM NaCl. The PTHR (QEEWETVM) peptide at a concentration of 0.875 mM was titrated into 50 μM SNX27 PDZ domain WT or H114A (supplemented with 50 μM VPS26A when required) protein solutions at 25°C. Data were processed using ORIGIN to extract the thermodynamic parameters ΔH and K_a ($1/K_d$) and the stoichiometry n. Here ΔG and ΔS were derived from $\Delta G = -RT \ln K_a$ and $\Delta G = \Delta H - T\Delta S$.

Histology and histomorphometry

Left proximal tibia and distal femur samples from 1-mo-old wild-type and knockout littermates were processed using a Leica TP1020 processor (Leica Biosystems, Nussloch, Germany) in preparation for either methyl methacrylate (MMA) or paraffin embedment according to standard protocol. Samples were sectioned using a Leica Biosystems RM2255 Automated Microtome for MMA-embedded samples or a Biocut 2035 at a thickness of 5 μm. Sections were stained for TRAP, Goldner's trichrome, Von Kossa, Safranin O, and PAS stains, and IHC was performed for collagen 2 according to standard protocols. Sections were then scanned using a Leica Biosystems Aperio ScanScope. Histomorphometric analysis was performed using BioQuant Osteo, version 13.2.6 (Bioquant Image Analysis, Nashville, TN).

Mineralization and ALP assay

Mineralization assays were conducted using 4×10^4 cells/well (24-well plate) in complete αMEM supplemented with osteogenic medium, that is, Control (complete αMEM with 50 μg/ml L-ascorbic acid and 2 mM β-glycerophosphate [Sigma-Aldrich]). Culture medium was replaced every other day and fixed after 21 d using 4% PFA. Bone nodules were stained using Alizarin Red S solution (Sigma-Aldrich), and bone nodule area (mm^2) was quantified using ImageJ (National Institutes of Health, Bethesda, MD). ALP activity was visualized using a Leukocyte Alkaline Phosphatase Kit (Sigma-Aldrich).

Cyclic AMP assay

Primary OBs were seeded into 96-well plate at 6×10^4 cells/well 24 h before the assay. Cells were serum starved for 1 h before the addition of IBMX (200 μM) for 30 min. Cells were then stimulated with PTH(1-34) (100 nM) for 5 min, and assay was subsequently performed using Cyclic AMP XP™ Assay Kit (Cell Signaling Technology) according to manufacturer's protocol. Absorbance was read at 450 nm. Four independent experiments were conducted.

Immunoblotting

Cultured HEK293 stable PTHR-expressing clones and primary OBs were serum starved for 1 h before stimulation with PTH(1-34) (100 nM) from 0 to 90 min, after a washout after 15 min of stimulation. Cells were washed with ice-cold 1× PBS and lysed in 1× RIPA buffer (50 mM Tris pH 7.4, 150 mM NaCl, 1% Nonidet P-40, 0.1% SDS, 1% sodium deoxycholate) supplemented with protease inhibitors: 1 mM PMSF (Sigma-Aldrich), 1 mM sodium orthovanadate, and 1× Complete Mini EDTA-free protease inhibitor cocktail (Roche Diagnostics, Basel, Switzerland). After ice incubation for 20 min, cell lysates were cleared by centrifugation at 15,000 rpm for 30 min at 4°C. A 10-μg amount of each protein sample was resolved by SDS–PAGE (8–12% polyacrylamide gels), and Western blot analyses were carried out with standard protocols using the indicated antibodies. Protein

Gene	Forward sequence	Reverse sequence	Accession number
ALP	cggatcctgaccaaaaacc	tcatgatgtccgtggtcaat	NM_007431.2
RUNX2	cgtgtcagcaaagcttctttt	ggctcacgtcgctcatct	NM_001146038.1
OSX	tgcttcccaatcctatttgc	agctcaggggaatcgag	NM_130458.3
RANKL	tgaagacacactacctgactcctg	cccacaatgtgttgcagttc	NM_011613.3
PTH1R	ggagacacctctctgaagttcc	cctggtctcagtcttctcatctg	NM_011199.2
MEPE	gatgcaggctgtgtctgttg	tgtcttcattcggcattgg	NM_053172.2
PHEX	tgcatctaccaaccagatacga	gcaccataactcagggatcg	EF194891.1
SNX27	gcagaatggtgagaagtttgtg	tcccggtaccgcttagaac	NM_029721.1
HMBS	cagtgatgaaagatgggcaac	aacagggacctggatggtg	NM_013551.2
ACTB	Taqman (#4352341E; Thermo Fisher Scientific)		

TABLE 2: Primer sequences used in this work.

bands were quantified by densitometry analysis using Photoshop 2014 (Adobe, San Jose, CA; data shown are representative of at least three independent experiments and expressed as mean ± SEM).

RNA and quantitative PCR

For quantifying gene expression, RNA samples were extracted using TRIzol (Thermo Fisher Scientific). First-strand synthesis was conducted using 1–2 µg of total RNA using SuperScript III RT Kit (Thermo Fisher Scientific) according to the manufacturer's protocol. Quantitative PCR was performed using a SensiMix II Probe Kit (Bioline Reagents, London, United Kingdom) and the Universal ProbeLibrary (Roche Diagnostics) and analyzed using a CFX Connect Real-Time System and CFX Manager Software (Bio-Rad, Hercules, CA). Relative fold expression was normalized to β-actin (ACTB; TaqMan) and hydroxymethylbilane synthase (HMBS) sample controls using the primer sequences shown in Table 2.

Skeletal staining and micro–computed tomography

Killed P5 mice were skinned, eviscerated, and fixed in 90% ethanol for 7 d and prepared for whole-mount staining with Alcian Blue and Alizarin Red S according to the protocol detailed in Linz *et al*. (2015). Whole-mount µCT of P5 mice was performed using SkyScan 1176 (Bruker, Kontich, Belgium) at 45 kV and 556 mA with a pixel size of 17.7 µm. For 0.1-mo-old mice, µCT was performed on the left proximal tibia and distal femur metaphysis and diaphysis for trabecular and cortical bone analysis, respectively, using SkyScan 1174 (Bruker) at 50 kV and 800 mA with a pixel size of 6.1 µm. All images were reconstructed using the SkyScan NRecon program version 1.1 and analyzed using SkyScan CTAn software (Bruker).

Statistical analysis and data presentation

Results were statistically analyzed using a two-tailed *t*-test using Prism 5 (GraphPad Software, La Jolla, CA). All data shown are representative of at least three independent experiments and expressed as mean ± SEM.

PDB accession codes

Structural data are deposited in the PDB under accession number 4Z8J. Raw diffraction data are available at the Diffraction Images Repository (http://xr-diffraction.imb.uq.edu.au).

ACKNOWLEDGMENTS

We thank T. J. Martin for the critical reading of the manuscript. All microscopy was carried out using facilities at the Centre for Microscopy, Characterisation, and Analysis, University of Western Australia. We also acknowledge the assistance with X-ray diffraction data collection of the resources and staff of the University of Queensland Remote Operation Crystallisation (UQ ROCX) and the Australian Synchrotron. This work was supported by grants from the National Health and Medical Research Council of Australia (APP1078280 to N.J.P., M.H.Z., and T.S.C. and APP1042082 and APP1058734 to B.M.C. and R.D.T.), the Department of Health Western Australia (to N.J.P., M.H.Z., and T.S.C.), and a UWA-UQ-A*STAR Trilateral Research Collaboration Award (N.J.P., R.D.T., B.M.T., and W.J.H.). B.M.C. was supported by a National Health and Medical Research Council Career Development Fellowship (APP1061574) and previously by an Australian Research Council Future Fellowship (FT100100027).

REFERENCES

Ardura JA, Wang B, Watkins SC, Vilardaga JP, Friedman PA (2011). Dynamic Na+-H+ exchanger regulatory factor-1 association and dissociation regulate parathyroid hormone receptor trafficking at membrane microdomains. J Biol Chem 286, 35020–35029.

Arighi CN, Hartnell LM, Aguilar RC, Haft CR, Bonifacino JS (2004). Role of the mammalian retromer in sorting of the cation-independent mannose 6-phosphate receptor. J Cell Biol 165, 123–133.

Aubry L, Guetta D, Klein G (2009). The arrestin fold: variations on a theme. Curr Genomics 10, 133–142.

Bakker AD, Klein-Nulend J (2012). Osteoblast isolation from murine calvaria and long bones. Methods Mol Biol 816, 19–29.

Balana B, Maslennikov I, Kwiatkowski W, Stern KM, Bahima L, Choe S, Slesinger PA (2011). Mechanism underlying selective regulation of G protein-gated inwardly rectifying potassium channels by the psychostimulant-sensitive sorting nexin 27. Proc Natl Acad Sci USA 108, 5831–5836.

Bisello A, Chorev M, Rosenblatt M, Monticelli L, Mierke DF, Ferrari SL (2002). Selective ligand-induced stabilization of active and desensitized parathyroid hormone type 1 receptor conformations. J Biol Chem 277, 38524–38530.

Bouxsein ML, Pierroz DD, Glatt V, Goddard DS, Cavat F, Rizzoli R, Ferrari SL (2005). beta-Arrestin2 regulates the differential response of cortical and trabecular bone to intermittent PTH in female mice. J Bone Miner Res 20, 635–643.

Cai L, Loo LS, Atlashkin V, Hanson BJ, Hong W (2011). Deficiency of sorting nexin 27 (SNX27) leads to growth retardation and elevated levels of N-methyl-D-aspartate receptor 2C (NR2C). Mol Cell Biol 31, 1734–1747.

Calvi LM, Sims NA, Hunzelman JL, Knight MC, Giovannetti A, Saxton JM, Kronenberg HM, Baron R, Schipani E (2001). Activated parathyroid hormone/parathyroid hormone-related protein receptor in osteoblastic cells differentially affects cortical and trabecular bone. J Clin Invest 107, 277–286.

Castro M, Nikolaev VO, Palm D, Lohse MJ, Vilardaga JP (2005). Turn-on switch in parathyroid hormone receptor by a two-step parathyroid hormone binding mechanism. Proc Natl Acad Sci USA 102, 16084–16089.

Chauvin S, Bencsik M, Bambino T, Nissenson RA (2002). Parathyroid hormone receptor recycling: role of receptor dephosphorylation and beta-arrestin. Mol Endocrinol 16, 2720–2732.
Collins BM (2008). The structure and function of the retromer protein complex. Traffic 9, 1811–1822.
Cullen PJ, Korswagen HC (2012). Sorting nexins provide diversity for retromer-dependent trafficking events. Nat Cell Biol 14, 29–37.
Damseh N, Danson CM, Al-Ashhab M, Abu-Libdeh B, Gallon M, Sharma K, Yaacov B, Coulthard E, Caldwell MA, Edvardson S, *et al.* (2015). A defect in the retromer accessory protein, SNX27, manifests by infantile myoclonic epilepsy and neurodegeneration. Neurogenetics 16, 215–221.
Datta NS, Abou-Samra AB (2009). PTH and PTHrP signaling in osteoblasts. Cell Signal 21, 1245–1254.
Emsley P, Lohkamp B, Scott WG, Cowtan K (2010). Features and development of Coot. Acta Crystallogr D Biol Crystallogr 66, 486–501.
Feinstein TN, Wehbi VL, Ardura JA, Wheeler DS, Ferrandon S, Gardella TJ, Vilardaga JP (2011). Retromer terminates the generation of cAMP by internalized PTH receptors. Nat Chem Biol 7, 278–284.
Ferrandon S, Feinstein TN, Castro M, Wang B, Bouley R, Potts JT, Gardella TJ, Vilardaga JP (2009). Sustained cyclic AMP production by parathyroid hormone receptor endocytosis. Nat Chem Biol 5, 734–742.
Ferrari SL, Behar V, Chorev M, Rosenblatt M, Bisello A (1999). Endocytosis of ligand-human parathyroid hormone receptor 1 complexes is protein kinase C-dependent and involves beta-arrestin2. Real-time monitoring by fluorescence microscopy. J Biol Chem 274, 29968–29975.
Gallon M, Clairfeuille T, Steinberg F, Mas C, Ghai R, Sessions RB, Teasdale RD, Collins BM, Cullen PJ (2014). A unique PDZ domain and arrestin-like fold interaction reveals mechanistic details of endocytic recycling by SNX27-retromer. Proc Natl Acad Sci USA 111, E3604–E3613.
Gallon M, Cullen PJ (2015). Retromer and sorting nexins in endosomal sorting. Biochem Soc Trans 43, 33–47.
Gardella TJ, Vilardaga JP (2015). International Union of Basic and Clinical Pharmacology. XCIII. The parathyroid hormone receptors-family B G protein-coupled receptors. Pharmacol Rev 67, 310–337.
Ghai R, Bugarcic A, Liu H, Norwood SJ, Skeldal S, Coulson EJ, Li SS, Teasdale RD, Collins BM (2013). Structural basis for endosomal trafficking of diverse transmembrane cargos by PX-FERM proteins. Proc Natl Acad Sci USA 110, E643–E652.
Ghai R, Mobli M, Norwood SJ, Bugarcic A, Teasdale RD, King GF, Collins BM (2011). Phox homology band 4.1/ezrin/radixin/moesin-like proteins function as molecular scaffolds that interact with cargo receptors and Ras GTPases. Proc Natl Acad Sci USA 108, 7763–7768.
Gidon A, Al-Bataineh MM, Jean-Alphonse FG, Stevenson HP, Watanabe T, Louet C, Khatri A, Calero G, Pastor-Soler NM, Gardella TJ, *et al.* (2014). Endosomal GPCR signaling turned off by negative feedback actions of PKA and v-ATPase. Nat Chem Biol 10, 707–709.
Gleason RJ, Akintobi AM, Grant BD, Padgett RW (2014). BMP signaling requires retromer-dependent recycling of the type I receptor. Proc Natl Acad Sci USA 111, 2578–2583.
Hanyu R, Wehbi VL, Hayata T, Moriya S, Feinstein TN, Ezura Y, Nagao M, Saita Y, Hemmi H, Notomi T, *et al.* (2012). Anabolic action of parathyroid hormone regulated by the beta2-adrenergic receptor. Proc Natl Acad Sci USA 109, 7433–7438.
Harterink M, Port F, Lorenowicz MJ, McGough IJ, Silhankova M, Betist MC, van Weering JR, van Heesbeen RG, Middelkoop TC, Basler K, *et al.* (2011). A SNX3-dependent retromer pathway mediates retrograde transport of the Wnt sorting receptor Wntless and is required for Wnt secretion. Nat Cell Biol 13, 914–923.
Hayashi H, Naoi S, Nakagawa T, Nishikawa T, Fukuda H, Imajoh-Ohmi S, Kondo A, Kubo K, Yabuki T, Hattori A, *et al.* (2012). Sorting nexin 27 interacts with multidrug resistance-associated protein 4 (MRP4) and mediates internalization of MRP4. J Biol Chem 287, 15054–15065.
Hirai T, Chagin AS, Kobayashi T, Mackem S, Kronenberg HM (2011). Parathyroid hormone/parathyroid hormone-related protein receptor signaling is required for maintenance of the growth plate in postnatal life. Proc Natl Acad Sci USA 108, 191–196.
Joubert L, Hanson B, Barthet G, Sebben M, Claeysen S, Hong W, Marin P, Dumuis A, Bockaert J (2004). New sorting nexin (SNX27) and NHERF specifically interact with the 5-HT4a receptor splice variant: roles in receptor targeting. J Cell Sci 117, 5367–5379.
Karaplis AC, Goltzman D (2000). PTH and PTHrP effects on the skeleton. Rev Endocr Metab Disord 1, 331–341.
Karaplis AC, Luz A, Glowacki J, Bronson RT, Tybulewicz VL, Kronenberg HM, Mulligan RC (1994). Lethal skeletal dysplasia from targeted disruption of the parathyroid hormone-related peptide gene. Genes Dev 8, 277–289.
Karim Z, Gerard B, Bakouh N, Alili R, Leroy C, Beck L, Silve C, Planelles G, Urena-Torres P, Grandchamp B, *et al.* (2008). NHERF1 mutations and responsiveness of renal parathyroid hormone. N Engl J Med 359, 1128–1135.
Kerr MC, Wang JT, Castro NA, Hamilton NA, Town L, Brown DL, Meunier FA, Brown NF, Stow JL, Teasdale RD (2010). Inhibition of the PtdIns(5) kinase PIKfyve disrupts intracellular replication of Salmonella. EMBO J 29, 1331–1347.
Kobayashi T, Chung UI, Schipani E, Starbuck M, Karsenty G, Katagiri T, Goad DL, Lanske B, Kronenberg HM (2002). PTHrP and Indian hedgehog control differentiation of growth plate chondrocytes at multiple steps. Development 129, 2977–2986.
Kraenzlin ME, Meier C (2011). Parathyroid hormone analogues in the treatment of osteoporosis. Nat Rev Endocrinol 7, 647–656.
Kronenberg HM (2003). Developmental regulation of the growth plate. Nature 423, 332–336.
Kular J, Tickner JC, Pavlos NJ, Viola HM, Abel T, Lim BS, Yang X, Chen H, Cook R, Hool LC, *et al.* (2015). Choline kinase beta mutant mice exhibit reduced phosphocholine, elevated osteoclast activity, low bone mass. J Biol Chem 290, 1729–1742.
Lanske B, Amling M, Neff L, Guiducci J, Baron R, Kronenberg HM (1999). Ablation of the PTHrP gene or the PTH/PTHrP receptor gene leads to distinct abnormalities in bone development. J Clin Invest 104, 399–407.
Lauffer BE, Melero C, Temkin P, Lei C, Hong W, Kortemme T, von Zastrow M (2010). SNX27 mediates PDZ-directed sorting from endosomes to the plasma membrane. J Cell Biol 190, 565–574.
Li X, Wang X, Zhang X, Zhao M, Tsang WL, Zhang Y, Yau RG, Weisman LS, Xu H (2013). Genetically encoded fluorescent probe to visualize intracellular phosphatidylinositol 3,5-bisphosphate localization and dynamics. Proc Natl Acad Sci USA 110, 21165–21170.
Linz A, Knieper Y, Gronau T, Hansen U, Aszodi A, Garbi N, Hammerling GJ, Pap T, Bruckner P, Dreier R (2015). ER stress during the pubertal growth spurt results in impaired long-bone growth in chondrocyte-specific ERp57 knockout mice. J Bone Miner Res 30, 1481–1493.
Liu L, Alonso V, Guo L, Tourkova I, Henderson SE, Almarza AJ, Friedman PA, Blair HC (2012). Na+/H+ exchanger regulatory factor 1 (NHERF1) directly regulates osteogenesis. J Biol Chem 287, 43312–43321.
Lohse MJ, Andexinger S, Pitcher J, Trukawinski S, Codina J, Faure JP, Caron MG, Lefkowitz RJ (1992). Receptor-specific desensitization with purified proteins. Kinase dependence and receptor specificity of beta-arrestin and arrestin in the beta 2-adrenergic receptor and rhodopsin systems. J Biol Chem 267, 8558–8564.
Loo LS, Tang N, Al-Haddawi M, Dawe GS, Hong W (2014). A role for sorting nexin 27 in AMPA receptor trafficking. Nat Commun 5, 3176.
Lunn ML, Nassirpour R, Arrabit C, Tan J, McLeod I, Arias CM, Sawchenko PE, Yates JR 3rd, Slesinger PA (2007). A unique sorting nexin regulates trafficking of potassium channels via a PDZ domain interaction. Nat Neurosci 10, 1249–1259.
Mahon MJ, Donowitz M, Yun CC, Segre GV (2002). Na(+)/H(+) exchanger regulatory factor 2 directs parathyroid hormone 1 receptor signalling. Nature 417, 858–861.
Martin TJ, Seeman E (2007). New mechanisms and targets in the treatment of bone fragility. Clin Sci (Lond) 112, 77–91.
McCauley LK, Martin TJ (2012). Twenty-five years of PTHrP progress: from cancer hormone to multifunctional cytokine. J Bone Miner Res 27, 1231–1239.
McCoy AJ, Grosse-Kunstleve RW, Adams PD, Winn MD, Storoni LC, Read RJ (2007). Phaser crystallographic software. J Appl Crystallogr 40, 658–674.
Miao D, He B, Jiang Y, Kobayashi T, Soroceanu MA, Zhao J, Su H, Tong X, Amizuka N, Gupta A, *et al.* (2005). Osteoblast-derived PTHrP is a potent endogenous bone anabolic agent that modifies the therapeutic efficacy of administered PTH 1–34. J Clin Invest 115, 2402–2411.
Miao D, He B, Karaplis AC, Goltzman D (2002). Parathyroid hormone is essential for normal fetal bone formation. J Clin Invest 109, 1173–1182.
Muhammad A, Flores I, Zhang H, Yu R, Staniszewski A, Planel E, Herman M, Ho L, Kreber R, Honig LS, *et al.* (2008). Retromer deficiency observed in Alzheimer's disease causes hippocampal dysfunction, neurodegeneration, and Abeta accumulation. Proc Natl Acad Sci USA 105, 7327–7332.
Ng PY, Cheng TS, Zhao H, Ye S, Sm Ang E, Khor EC, Feng HT, Xu J, Zheng MH, Pavlos NJ (2013). Disruption of the dynein-dynactin complex unveils motor-specific functions in osteoclast formation and bone resorption. J Bone Miner Res 28, 119–134.
Pavlos NJ, Gronborg M, Riedel D, Chua JJ, Boyken J, Kloepper TH, Urlaub H, Rizzoli SO, Jahn R (2010). Quantitative analysis of synaptic vesicle

Rabs uncovers distinct yet overlapping roles for Rab3a and Rab27b in Ca2+-triggered exocytosis. J Neurosci 30, 13441–13453.
Qiu T, Wu X, Zhang F, Clemens TL, Wan M, Cao X (2010). TGF-beta type II receptor phosphorylates PTH receptor to integrate bone remodelling signalling. Nat Cell Biol 12, 224–234.
Schipani E, Kruse K, Juppner H (1995). A constitutively active mutant PTH-PTHrP receptor in Jansen-type metaphyseal chondrodysplasia. Science 268, 98–100.
Schipani E, Langman CB, Parfitt AM, Jensen GS, Kikuchi S, Kooh SW, Cole WG, Juppner H (1996). Constitutively activated receptors for parathyroid hormone and parathyroid hormone-related peptide in Jansen's metaphyseal chondrodysplasia. N Engl J Med 335, 708–714.
Seaman MN (2012). The retromer complex—endosomal protein recycling and beyond. J Cell Sci 125, 4693–4702.
Shenolikar S, Voltz JW, Minkoff CM, Wade JB, Weinman EJ (2002). Targeted disruption of the mouse NHERF-1 gene promotes internalization of proximal tubule sodium-phosphate cotransporter type IIa and renal phosphate wasting. Proc Natl Acad Sci USA 99, 11470–11475.
Shi H, Rojas R, Bonifacino JS, Hurley JH (2006). The retromer subunit Vps26 has an arrestin fold and binds Vps35 through its C-terminal domain. Nat Struct Mol Biol 13, 540–548.
Sims NA, Martin TJ (2014). Coupling the activities of bone formation and resorption: a multitude of signals within the basic multicellular unit. Bonekey Rep 3, 481.
Sneddon WB, Syme CA, Bisello A, Magyar CE, Rochdi MD, Parent JL, Weinman EJ, Abou-Samra AB, Friedman PA (2003). Activation-independent parathyroid hormone receptor internalization is regulated by NHERF1 (EBP50). J Biol Chem 278, 43787–43796.
Sorkin A, von Zastrow M (2009). Endocytosis and signalling: intertwining molecular networks. Nat Rev Mol Cell Biol 10, 609–622.
Steinberg F, Gallon M, Winfield M, Thomas EC, Bell AJ, Heesom KJ, Tavare JM, Cullen PJ (2013). A global analysis of SNX27-retromer assembly and cargo specificity reveals a function in glucose and metal ion transport. Nat Cell Biol 15, 461–471.
Teasdale RD, Collins BM (2012). Insights into the PX (phox-homology) domain and SNX (sorting nexin) protein families: structures, functions and roles in disease. Biochem J 441, 39–59.
Temkin P, Lauffer B, Jager S, Cimermancic P, Krogan NJ, von Zastrow M (2011). SNX27 mediates retromer tubule entry and endosome-to-plasma membrane trafficking of signalling receptors. Nat Cell Biol 13, 715–721.
Valdes JL, Tang J, McDermott MI, Kuo JC, Zimmerman SP, Wincovitch SM, Waterman CM, Milgram SL, Playford MP (2011). Sorting Nexin 27 regulates trafficking of a PAK interacting exchange factor (betaPIX)-G-protein-coupled receptor kinase interacting protein (GIT) complex via a PDZ domain interaction. J Biol Chem 286, 39403–39416.
Vilardaga JP, Gardella TJ, Wehbi VL, Feinstein TN (2012). Non-canonical signaling of the PTH receptor. Trends Pharmacol Sci 33, 423–431.
Vilardaga JP, Jean-Alphonse FG, Gardella TJ (2014). Endosomal generation of cAMP in GPCR signaling. Nat Chem Biol 10, 700–706.
Vilarino-Guell C, Wider C, Ross OA, Dachsel JC, Kachergus JM, Lincoln SJ, Soto-Ortolaza AI, Cobb SA, Wilhoite GJ, Bacon JA, *et al.* (2011). VPS35 mutations in Parkinson disease. Am J Hum Genet 89, 162–167.
von Zastrow M, Sorkin A (2007). Signaling on the endocytic pathway. Curr Opin Cell Biol 19, 436–445.
Wang B, Bisello A, Yang Y, Romero GG, Friedman PA (2007). NHERF1 regulates parathyroid hormone receptor membrane retention without affecting recycling. J Biol Chem 282, 36214–36222.
Wang B, Yang Y, Friedman PA (2008). Na/H exchange regulatory factor 1, a novel AKT-associating protein, regulates extracellular signal-regulated kinase signaling through a B-Raf-mediated pathway. Mol Biol Cell 19, 1637–1645.
Wang X, Huang T, Zhao Y, Zheng Q, Thompson RC, Bu G, Zhang YW, Hong W, Xu H (2014). Sorting nexin 27 regulates Abeta production through modulating gamma-secretase activity. Cell Rep 9, 1023–1033.
Wang X, Zhao Y, Zhang X, Badie H, Zhou Y, Mu Y, Loo LS, Cai L, Thompson RC, Yang B, *et al.* (2013). Loss of sorting nexin 27 contributes to excitatory synaptic dysfunction by modulating glutamate receptor recycling in Down's syndrome. Nat Med 19, 473–480.
Weinman EJ, Mohanlal V, Stoycheff N, Wang F, Steplock D, Shenolikar S, Cunningham R (2006). Longitudinal study of urinary excretion of phosphate, calcium, and uric acid in mutant NHERF-1 null mice. Am J Physiol Renal Physiol 290, F838–F843.
Weinstein LS, Chen M, Xie T, Liu J (2006). Genetic diseases associated with heterotrimeric G proteins. Trends Pharmacol Sci 27, 260–266.
Wheeler DS, Barrick SR, Grubisha MJ, Brufsky AM, Friedman PA, Romero G (2011). Direct interaction between NHERF1 and Frizzled regulates beta-catenin signaling. Oncogene 30, 32–42.
Wu JY, Aarnisalo P, Bastepe M, Sinha P, Fulzele K, Selig MK, Chen M, Poulton IJ, Purton LE, Sims NA, *et al.* (2011). Gsalpha enhances commitment of mesenchymal progenitors to the osteoblast lineage but restrains osteoblast differentiation in mice. J Clin Invest 121, 3492–3504.
Ye F, Zhang M (2013). Structures and target recognition modes of PDZ domains: recurring themes and emerging pictures. Biochem J 455, 1–14.
Yin X, Murphy SJ, Wilkes MC, Ji Y, Leof EB (2013). Retromer maintains basolateral distribution of the type II TGF-beta receptor via the recycling endosome. Mol Biol Cell 24, 2285–2298.
Zimprich A, Benet-Pages A, Struhal W, Graf E, Eck SH, Offman MN, Haubenberger D, Spielberger S, Schulte EC, Lichtner P, *et al.* (2011). A mutation in VPS35, encoding a subunit of the retromer complex, causes late-onset Parkinson disease. Am J Hum Genet 89, 168–175.